JAGIELLONIAN UNIVERSITY

FACULTY OF PHYSICS, ASTRONOMY AND APPLIED COMPUTER SCIENCE
MARIAN SMOLUCHOWKI INSTITUTE OF PHYSICS

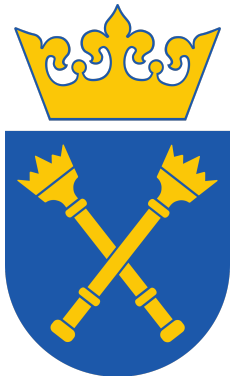

Doctoral dissertation

Production of ^{99m}Tc/^{99}Mo radioisotopes using proton and electron beams

Arshiya Anees Ahmed

Supervisor:
prof. dr hab. Andrzej Magiera

Auxiliary supervisor:
dr Aleksandra Wrońska

Cracow 2021

Contents

Abstract

Radioisotopes are employed in nuclear medicine for diagnostic imaging, therapy, and sterilization of equipment. However, the search and utilization of unique and novel therapeutic radioisotopes is required due to the continuous development of nuclear medicine and treatment methods. In nuclear medicine, ^{99m}Tc is the most frequently used radioisotope. It is employed in 80% of all nuclear medicine procedures.

In this thesis, the production routes were studied for the formation of medically important radioisotope ^{99}Mo/^{99m}Tc generators using accelerator facilities in Cracow, Poland. The medical radionuclides were produced using ^{nat}Mo targets and proton and electron beams. The nuclear reaction cross section $\sigma(E)$, and target yield, $TY(E)$, were obtained experimentally and used to discuss the feasibility of optimal large-scale production conditions for the ^{99}Mo/^{99m}Tc radioisotope generator. Long-lived radioimpurities produced in the ^{nat}Mo target by (p, x) and (γ, x) reactions were also investigated.

Dedication

I dedicate this thesis to the Almighty, to the Supremacy, and the Redeemer of my soul,

To my loving parents Mr. Anees Ahmed and Mrs. Mohsina Banu whose constant support, love, encouragement and prays of day and night make me able to get such success and honor, and to all my teachers who encouraged me to reach here.

Acknowledgements

Many people have bestowed their blessings and heartfelt support on me in the successful completion of this dissertation, and I would like to take this opportunity to thank everyone who has been involved directly or indirectly with this thesis. At first, I would like to express my deep gratitude to my academic parents, Prof. Andrzej Magiera (supervisor) and Dr. Aleksandra Wrońska (co-supervisor), for accepting my research proposal and helped me to make this work possible. I thank them for their constant guidance, advice, and support which kept me going through every stage of my Ph.D. I am grateful to all my collaborators from SOLARIS and IFJ PAN, for their support during experiments and helped me to carry this research work. I am grateful to student lab assistants Mr. Adam Mucha and Artur Michałek for always keeping the detector ready for the measurements and helping me set up the detector system. I thank my colleagues for their help and support. I like to thank Kasia Rusiecka for teaching ROOT without which the research would have been impossible, and for long research and non-research-related conversations. I appreciate my friend Swathi karanth's help in programming. I want to thank Late. Prof. Jerzy Jastrzębski and Dr. Mateusz Sitarsz from the University of Warsaw who helped me to understand the research work and methodology. There were many ups and downs during this period and my friends were always there for me, as my support system. I would like to thank each friend of mine who was there at my back and brought so many cherishable memories in my life. I especially want to thank my dear Shivani for her endless support and understanding. I would like to express my special thanks to Prof. S.B. Gudennavar and Prof. S.G. Bubbly for sowing the seed of research in me from my master's study and being my guiding light. Last but not least, I want to wholeheartedly thank my brother Arfath for his unconditional love and support.

Chapter 1

Introduction

Radioisotopes are employed in a variety of applications in nuclear medicine, including research, imaging, therapy, radiopharmaceuticals, and equipment sterilization [1, 2]. Over 40 million medical procedures involving radioisotopes are conducted each year world-wide, with an expected annual increase rate of 5%. About one out of every 50 people in developed countries uses diagnostic nuclear medicine each year, and about one-tenth of this involves radioisotope therapy [1].

Radioisotopes which are used in medicine for both diagnostic and therapeutic purposes need to be guided to reach the place in the human body, where they are expected to act. For this purpose, radioisotopes are bond to biologically active molecules called biomolecules and this binding process is called radiolabeling. For scanning, radiotracers are used. Depending on the purpose of a scan, different biomolecules are employed. Some tracers make use of chemicals that connect with a specific protein or sugar in the body, also patient's own cells can be used as a biomolecule. In most nuclear medicine diagnostic investigations, the radioactive tracer is given to the patient through intravenous injection. Other ways to administer a radioactive tracer are through inhalation, oral ingestion, or direct injection into an organ of interest. The method of tracer administration is determined by the disease process being investigated.

Tracers that have been approved are referred as radiopharmaceuticals because they must meet the Food and Drug Administration's (FDA) exacting standards for safety and appropriate performance for approved clinical use [3]. The tracers accumulate in specific tissues and organs by physiological/metabolic processes in the body. Thus, radioactive emissions from the

tracers can be utilized to noninvasively image these processes (diagnosis) or kill cells in areas where radionuclides have accumulated (therapy).

Researchers from University of Pennsylvania, David Khul and Roy Edwards for years worked on a new method for detecting radioactive isotopes in the body using a tomographic imaging technique [4]. This work led to the development of today's most reliable diagnostic technique Single Photon Emission Computed Tomography (SPECT).

SPECT creates three-dimensional (3D) images of tissues and organs using radionuclides that emit gamma rays. ^{99m}Tc is the most commonly used radionuclide in MBq quantity for a single diagnosis [5]. A gamma camera is used to detect individual gamma rays emitted by the decay of these radiotracers (i.e. single photon emission). The basic principle behind the SPECT system relying on the rotating camera concept is to collect a series of planar images while rotating the camera through either 180 or 360 degrees around the patient. 3D SPECT images are then generated by a computer program using a large number of 2D images captured from different angles. Most of the gamma cameras used in present SPECT systems are based on single or multiple NaI(Tl) scintillation detectors [6], though semiconductor detectors become more and more common, offering better performance [7]. Fig. 1.1 shows the schematic of a SPECT system.

Even though radioisotopes occur naturally (like uranium ^{235}U and radium ^{226}Ra), most of the medically important radioisotopes are produced artificially in nuclear reactors or cyclotrons [1]. In 1957, Brookhaven National Laboratory (BNL) invented the ^{99}Mo/^{99m}Tc generator system. Technetium-99m (^{99m}Tc) produced through this generator has become the most commonly used radioisotope in medicine. It is exploited in almost 85% of nuclear medicine procedures and has an annual market share of approximately $ 500 million [1]. Since ^{99m}Tc and its parent molybdenum radioisotope (^{99}Mo) have short half-lives (6 and 66 hours, respectively), thus they cannot be stored up. Therefore, they need to be produced and processed daily to meet the global demand [8]. The majority of ^{99}Mo is produced either through the reactor-based nuclear fission reaction $^{235}\mathrm{U}(n, f)^{99}\mathrm{Mo}$ using enriched uranium-235, or by the neutron capture reaction $^{98}\mathrm{Mo}(n, \gamma)^{99}\mathrm{Mo}$. The latter is favourable if the target is irradiated with a high-density neutron flux [9]. The neutron-induced fission reaction of enriched ^{235}U produces, along with the desired ^{99}Mo a lot of long-lived radioactive waste which amounts to about 50 Ci per 1 Ci of ^{99}Mo [10]. This raises a number of safety and security problems.

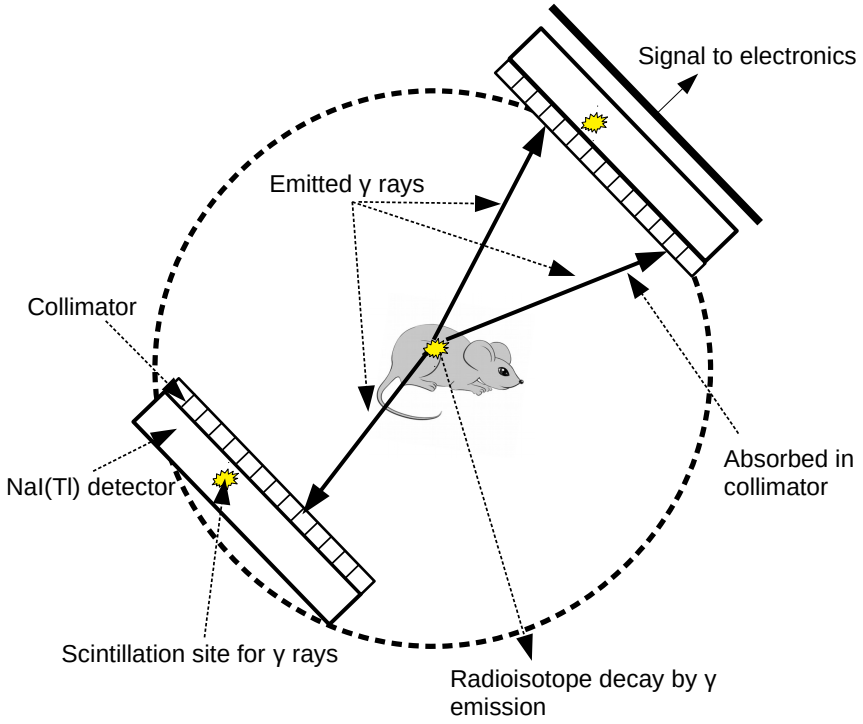

Figure 1.1: Schematics of SPECT system (figure taken from [6]).

Until early 2010, the National Research Universal (NRU) reactor in Chalk River, Ontario, U.S.A. and the High Flux Reactor (HFR) in Petten, Netherlands, were used to supply 60% of the global demand for ^{99}Mo [11]. The former reactor was on standby, only to resume production in the case of a supply shortage during 2018 [1]. Later in the same year, it was shut down completely. The HFR was closed in 2010 due to water leakage [11]. Most of the supply formerly produced at NRU is set to be produced at the University of Missouri Research Reactor (MURR), which is a 10-MW pool-type reactor, and the production process makes use of low enriched uranium (LEU) targets [1]. Additionally to MURR, a network of 11 cyclotrons across Canada also deliver ^{99m}Tc [12] and help satisfy the demand locally,exploiting enriched ^{100}Mo as a target that can only be purchased from Russia [1, 12]. The cost

of the cyclotron-produced ^{99m}Tc is estimated to be three to ten times higher than when produced in reactors.

Due to their aging, many of the reactors that are currently used to produce radioactive ingredients for radiopharmaceuticals are scheduled for shutdown within the next few years. This makes the reactor-based production unreliable over the longer term [13]. Therefore, other production paths, which do not require the use of reactors, are sought for. One of the possible options is the use of accelerators, which have a number of advantages compared to reactors for radionuclei production such as lower operating cost, safety, and a reduced amount of radioactive by-products. Accelerators can be located close to the places where the isotopes are used, thus minimizing the transportation time. Many accelerators with several MeV proton energy range are available for radioisotope production for medical applications. ^{99}Mo can be produced via proton induced reaction through $^{100}\mathrm{Mo}(p,pn)^{99}\mathrm{Mo}$ and $^{100}\mathrm{Mo}(p,2n)^{99m}\mathrm{Tc}$ reactions. The proton energy range of $10-25$ MeV is the optimal for production of ^{99m}Tc and $15-35$ MeV for the $^{100}\mathrm{Mo}(p,pn)^{99}\mathrm{Mo}$ reaction. Deuteron beams can also be used to produce radioisotopes from ^{nat}Mo via the $^{98,100}\mathrm{Mo}(d,x)$ reaction. Currently, in several centers, radioisotopes are being produced using proton and deuteron beams accelerated by cyclotrons [14].

^{99}Mo can also be produced through the $^{100}\mathrm{Mo}(\gamma,n)^{99}\mathrm{Mo}$ reaction. Linear electron accelerators (linacs), however, are in practice not exploited for this purpose, although many research studies showed this option would be feasible [9, 10, 13, 15–21].

The thesis aims to explain the nuclear physics behind the generation of radioisotopes. ^{99}Mo/^{99m}Tc generator was chosen to study and meet the above mentioned purpose. Production cross section and target yield of ^{99}Mo/^{99m}Tc radioisotopes along with the long-lived radio-impurities studied with the use of accelerator facilities located in Cracow, Poland.

Chapter 2

Theoretical background

2.1 Radioactivity and reaction cross section

In the nineteenth century, an Englishman named John Dalton proposed his atomic theory, which stated that all atoms of the same element were identical. This went unchallenged for 100 years, until experiments by the British chemist Frederick Soddy proved conclusively that the element neon was made up of two types of atoms. Chemically, they were all the same, but some had an atomic weight of 20 and others had an atomic weight of 22. He coined the term "isotope" to refer to one of two or more atoms with the same atomic number but different atomic weights [22].

Radioisotopes are isotopes that are unstable, i.e., spontaneously emit radiation. They occur naturally or can be created artificially, e.g., by bombarding suitable targets with neutrons, which are presently abundant in atomic reactors. However, certain radioisotopes are more satisfactorily produced by the irradiation of protons, deuterons, photons, or other subatomic particles, given their sufficiently high energy.

Radioactivity has a feature that is virtually unaffected by any of the factors that are used to control the rate of chemical reactions, such as temperature and pressure. The structure of the unstable (decaying) nucleus appears to be the only factor influencing the rate of radioactive decay. Each radioisotope has its own half-life, which is the amount of time it takes for half of the nuclei present in a sample to decay. The half-lives range from fractions of a second to millions of years, depending on the nuclide and decay type. The majority of radioisotopes created artificially are short-lived. This has two con-

sequences. First, it means that only a small amount of material is required to obtain a significant number of disintegrations, since the disintegration rate is inversely proportional to the half-life. Second, after 10 half-lives, the activity will have decreased by factor of 1024, and the amount of radioactive material will be so small that it is usually no longer significant.

Since radioisotopes are unstable, their mean life-time τ is inversely related to the decay constant λ:

$$\tau = \frac{1}{\lambda}. \tag{2.1}$$

Furthermore, the radioisotope half-life $T_{1/2}$ is given as:

$$T_{1/2} = \frac{\ln 2}{\lambda}. \tag{2.2}$$

The unstable radionuclide loses energy through decay (in the form of ionising radiation), generally the radioactive nucleus emits radiations through $\beta^{+/-}$ decay, α decay, electron capture (EC), isomeric transition (IT), and the spontaneous fission process. Any radioactive decay process other than IT leaves the residual nucleus excited. The de-excitation proceeds via emission of photons (γ rays) of energies E_γ and with intensities I_γ. Some isotopes can have an isomeric metastable state, which represents the excited state of nuclei with $T_{1/2}$ which is identical to other decay half-lives. The activity $A(t)$ of radioisotope 1 is defined as the number of decays dN_1 of N_1 nuclei in the given period dt:

$$\frac{dN_1(t)}{dt} = -A(t) = -\lambda \cdot N_1(t), \tag{2.3}$$

and it is expressed in becquerel [Bq]. The solution of that equation is given by

$$A(t) = A(0) \cdot e^{-\lambda t}, \tag{2.4}$$

where $A(0)$ is the activity at the beginning of the decay process. If the decay product is still unstable, then the second decay occurs. The rate at which radioisotope 2 is produced is

$$\frac{dN_2(t)}{dt} = -\lambda_2 \cdot N_2(t) + P_{dec} \cdot \lambda_1 \cdot N_1(t), \tag{2.5}$$

where P_{dec} is the probability at which radionuclide 1 decay to radionuclide 2. Solving for $A_2(t)$

$$A_2(t) = A_1(0) \cdot \frac{\lambda_2 \cdot P_{dec}}{\lambda_2 - \lambda_1}(e^{-\lambda_1 \cdot t} - e^{-\lambda_2 \cdot t}) + A_2(0) \cdot e^{-\lambda_2 \cdot t}. \tag{2.6}$$

The Eqn. 2.6 gives the solution for the so-called "parent-daughter" decay.

2.1.1 Nuclear reaction cross section

Cross section is the likelihood that a given atomic nucleus or subatomic particle would exhibit a specific reaction (for example, absorption, scattering, or fission) in relation to a specific species of incident particle in nuclear or subatomic particle physics. The barn [b] (equivalent to 10^{-24} cm^2) is the reaction cross section unit. The cross section of a reaction depends on the energy of the colliding particles and the type of reaction.

Integration of the differential cross section $\frac{d\sigma}{d\Omega}$ over the full solid angle yields the total cross section (σ):

$$\sigma = \int_{4\pi} \frac{d\sigma}{d\Omega} d\Omega = \int_0^{2\pi} d\varphi \int_0^{\pi} \frac{d\sigma}{d\Omega} sin\theta d\theta, \tag{2.7}$$

where θ is the scattering angle of the particle and $d\Omega = sin\theta d\theta d\varphi$ the element of the solid angle.

2.2 Production of radionuclides using charged particles

Let us consider a solid target which is in the form of a single layered thin foil, which contains N_{st} stable nuclei of σ cross section for the interaction and S is the surface of the target as shown in the Fig. 2.1. Then the probability of the interaction is given by

$$P_{int} = \frac{\sigma \cdot N_{st}}{S}. \tag{2.8}$$

If F be the flux of the charged projectiles, impinging perpendicular on the target, then the nuclear reaction rate R is defined as

$$R = P_{int} \cdot F = \frac{\sigma \cdot N_{st} \cdot F}{S}. \tag{2.9}$$

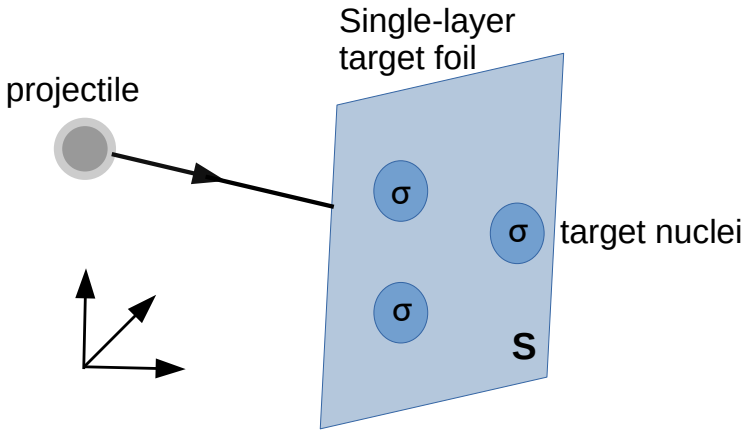

Figure 2.1: Projectile impinging on the single-layer foil of surface S, with σ cross section of N_{st} target nuclei.

When the interaction between the projectile and the target nucleus occurs, a new nuclide is produced. If it is radioactive, it has a non-zero λ decay probability. The rate at which radioactive nuclei are formed and decay in the time dt is:

$$\frac{dN_{rad}(t)}{dt} = \frac{N_{st} \cdot \sigma \cdot F}{S} - \lambda \cdot N_{rad}. \tag{2.10}$$

If N_{st} is assumed to be constant during the irradiation time (t_{irr}), the above equation has the following solution:

$$N_{rad}(t_{\mathrm{irr}}) = \frac{N_{st} \cdot \sigma \cdot F}{S \cdot \lambda} \cdot (1 - e^{-\lambda \cdot t_{\mathrm{irr}}}). \tag{2.11}$$

Consequently, the activity A_{EOB} at the end of bombardment (irradiation) can be calculated by differentiation of the above equation

$$A_{\mathrm{EOB}}(t_{\mathrm{irr}}) = \frac{N_{st} \cdot \sigma \cdot F}{S} \cdot (1 - e^{-\lambda \cdot t_{\mathrm{irr}}}). \tag{2.12}$$

Let us introduce $N = N_{st}/S$ as the areal density of target nuclei. Then the equation looks like

$$A_{\mathrm{EOB}}(t_{\mathrm{irr}}) = N \cdot \sigma \cdot F \cdot (1 - e^{-\lambda \cdot t_{\mathrm{irr}}}). \tag{2.13}$$

The charged particle flux delivered by the particle accelerator is the same as the beam intensity I. If we know the total charge q delivered by the beam

during the time of irradiation t_{irr}, we can calculate the beam current

$$I = \frac{q}{t_{\text{irr}}}. \tag{2.14}$$

If the beam particles have the charge of Ze each, where e is the elementary charge, then the projectile flux is related to the beam current by:

$$F = \frac{q}{Z \cdot e \cdot t_{\text{irr}}} = \frac{I}{Z \cdot e} \tag{2.15}$$

which can be reduced to

$$F\ [\text{s}^{-1}] \approx 6.3 \cdot 10^{12} \cdot \frac{I\ [\mu\text{A}]}{Z}. \tag{2.16}$$

The number of nuclei per unit area N is proportional to the number of stable nuclei per unit mass (n_{st}), the target thickness d and the density of the target material ρ:

$$N = d \cdot \rho \cdot n_{st}. \tag{2.17}$$

On the other hand,

$$n_{st} = H \cdot \frac{N_A}{M}, \tag{2.18}$$

where N_A is Avogadro's number, M represents the molar mass of the target, and H is the isotopic abundance of the target. The areal density x [g/cm^2] is $x = d \cdot \rho$.

Now, substituting N in Eqn. 2.13 using the above relationships, we obtain:

$$A_{\text{EOB}}(t_{\text{irr}}) = H \cdot \frac{N_A}{M} \cdot \frac{I}{Z \cdot e} \cdot x \cdot \sigma \cdot (1 - e^{-\lambda \cdot t_{\text{irr}}}). \tag{2.19}$$

If the target is thick such that the energy loss of the charged particle is not negligible, then the stopping power of the projectile in the target material (dE/dx) and energy-dependent cross section need to be accounted for when finding A_{EOB}:

$$A_{\text{EOB}}(t_{\text{irr}}) = H \cdot \frac{N_A}{M} \cdot \frac{I}{Z \cdot e} \cdot (1 - e^{-\lambda \cdot t_{\text{irr}}}) \cdot \int_{E_0}^{E_{max}} \frac{\sigma(E)}{dE/dx} dE. \tag{2.20}$$

During the production of a specific radioisotope, it is essential to know the efficiency of the production to optimize the irradiation conditions. Target

yield (TY) is a parameter which helps to optimise the production. TY is defined as:

$$TY = \frac{A_{\mathrm{EOB}}}{I \cdot t_{\mathrm{irr}}}. \tag{2.21}$$

If the time of irradiation is long such that the produced activity decays during the irradiation, then A_{EOB} will be lower than expected, after considering the decay factor then the above equation changes as:

$$TY = \frac{A_{\mathrm{EOB}} \cdot \lambda}{I \cdot (1 - e^{-\lambda \cdot t_{\mathrm{irr}}})}. \tag{2.22}$$

Comparing Eqn. 2.20 and 2.22 and solving for TY:

$$TY = \frac{H \cdot N_A \cdot \lambda}{M \cdot Z \cdot e} \cdot \int_{E_0}^{E_{max}} \frac{\sigma(E)}{dE/dx} dE. \tag{2.23}$$

2.3 Production of radioisotopes using photons

In general, photo-nuclear reactions can be explained as two-step phenomena. At first, the nucleus gets excited by absorbing a photon. In the next step, the excited nucleus de-excites by the emission of photons, neutrons, or charged particles.

Below 10 MeV photon energy, photon absorption by the nucleus usually leads to an excitation of a single nuclear level, and the excitation energy is insufficient to allow particle emission. In the photon energy range between 10 to 30 MeV, a giant dipole resonance (GDR) is observed, which is a collective excitation that is likely to result in the emission of single nucleons. Hence, this energy range is favourable for radioisotope production. Photons with energies above 30 MeV are likely to induce unwanted few-nucleon emission at the cost of a reduced single nucleon emission. This range is therefore less favourable. However, when the photon energy is higher than 140 MeV, photo-absorption cross section increases, since this is a threshold energy of π-meson production [13].

Large cross section of photoinduced nuclear reactions leads to a large total induced activity. However, the photoneutron reaction which leads to the production of a particular radioisotope of interest is small fraction of all photonuclear reactions, hence the nuclei of interest are produced together

with other impurities. These can be eliminated, thereby increasing the specific activity of the radionuclide of interest, by separating the daughter nuclei from the parent. If the parent and daughter are for different elements then it is easy to separate them. However, the parent-daughter nuclides are of the same chemical element and thus difficult to separate. In Ref. [13], the authors suggest to use the kinematic recoiling method to separate the parent and daughter nuclei. In the kinematic recoiling method, when a high energy photon removes a neutron from the nucleus of the target, some of the produced daughter nuclei have a kinetic energy sufficient to escape from the target. Subsequently, the recoils can be caught in the other material, so-called catcher, that is in contact with the target. As the target thickness decreases, the probability of such an escapement increases.

If the number of atoms in the target is N_{st} and I represents the convolution of photon flux and the cross section, then the daughter nuclei production rate $N^{'}$ is given by

$$N' = N_{st} \cdot I, \tag{2.24}$$

where I is expressed as

$$I = \int_{E_{th}}^{E_{max}} \phi(E_\gamma) \cdot \sigma(E_\gamma) dE_\gamma. \tag{2.25}$$

Here, $\phi(E_\gamma)$ is the photon flux and $\sigma(E_\gamma)$ is the reaction cross section.

The value of integral I can be calculated using a photonuclear cross section and the energy distribution of the photon flux determined either via measured or Monte-Carlo simulations. Through this method $N^{'}$ is estimated and finally the activity at the end of the irradiation can be calculated as follows:

$$A = N' \cdot (1 - e^{-\lambda t_{\mathrm{irr}}}). \tag{2.26}$$

Chapter 3

Experimental environment

In this work, the production of medical radioisotopes is studied with the use of two accelerator facilities located in Cracow, Poland: Cyclotron Centre Bronowice (CCB), is a part of the Institute of Nuclear Physics, Polish Academy of Sciences, and the National Synchrotron Radiation Centre SOLARIS. Both accelerator facilities are described in this chapter, along with the detectors used for the measurements.

3.1 Cyclotron AIC-144

Proton irradiations were conducted using the external beam of AIC-144 cyclotron located at Institute of Nuclear Physics, Polish Academy of Sciences, Cracow, Poland. The cyclotron is an isochronous type which is capable of accelerating protons in the form of a highly focused beam of 60 MeV energy and the intensity of 80 nA. The cyclotron delivers mono-energetic proton beam of fixed energy. To achieve the desired beam energy, one needs to use low-Z material as an energy degrader. The photo of the AIC-144 cyclotron is shown in Fig. 3.1.

3.2 Synchrotorn SOLARIS

To study the photon-induced reactions, we used an accelerated electron beam from the linac injector of the National Synchrotron Radiation Centre, SOLARIS, Jagiellonian University, Cracow, Poland. Fig 3.2 (a) shows the schematic of SOLARIS linac system and we installed the target just at

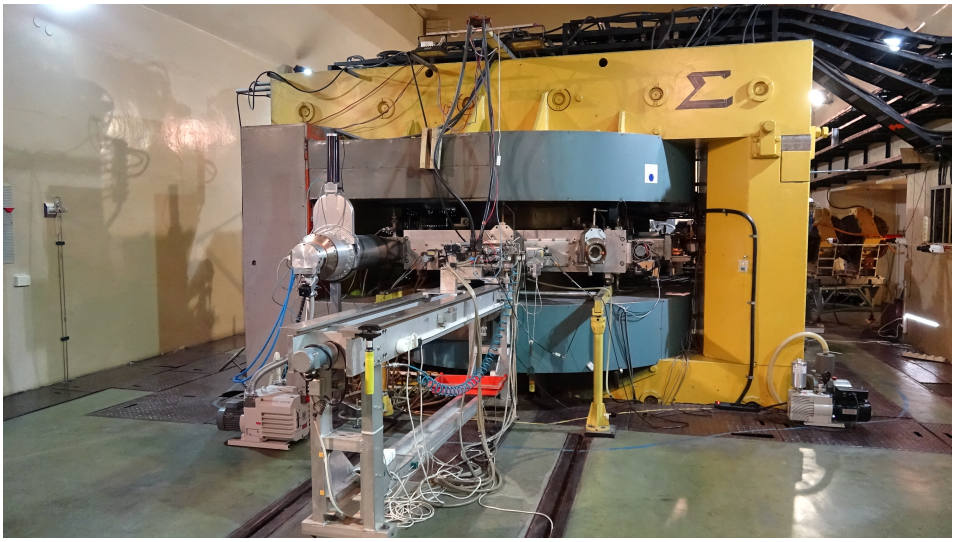

Figure 3.1: AIC-144 cyclotron of Cyclotron Centre Bronowice, Cracow Poland.

the end of the linac end flange as shown in Fig 3.2 (b). The facility is capable of accelerating a beam of electrons up to 550 MeV with a maximum charge of electron bunch of 0.2 nC. Specific beam conditions during each irradiation will be discussed later in detail.

3.3 HPGe detectors

3.3.1 Semiconductor detectors - operation principle

Radiation detectors are of vital importance in nuclear medicine. They are used in a broad range of applications, such as dosimetry, SPECT/PET imaging or determination of activity in the irradiated target material. A radiation detector is a sensor which produces a signal when radiation interacts with the detector material and the signal can be processed electronically to extract the required information. For X-rays and γ radiation, the main interaction mechanisms are photoelectric effect, Compton scattering, and e^+e^- pair production. The cross sections of those processes depend on the detector medium properties and the radiation energy. There are different types of radiation detectors: gas detectors, semiconductor detectors, and scintillating detector. In

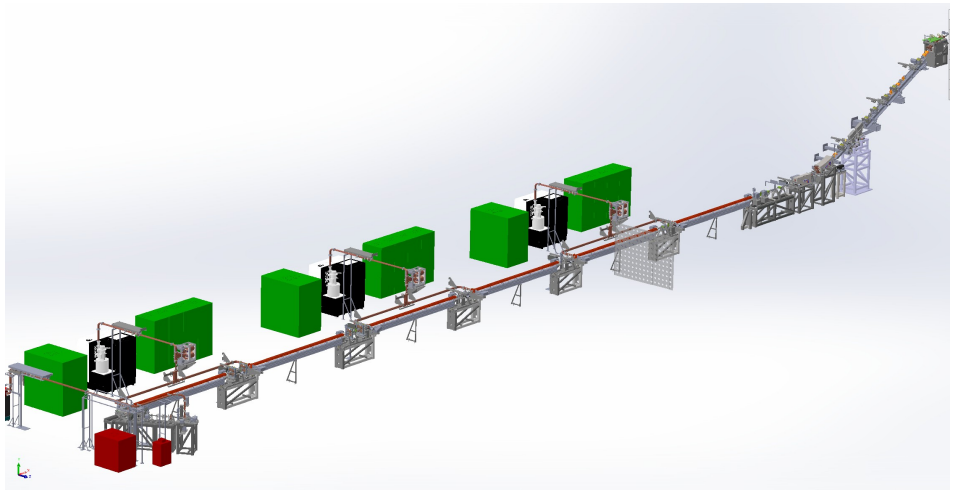

(a)

(b)

Figure 3.2: (a): Schematics of the linac at SOLARIS, (b): Side view of the linac injector with the target position indicated.

this study, only semiconductor detectors were employed due to their superior energy resolution, thus other types of detectors are not discussed here. Fig. 3.3 shows the working principle of a semiconductor detector.

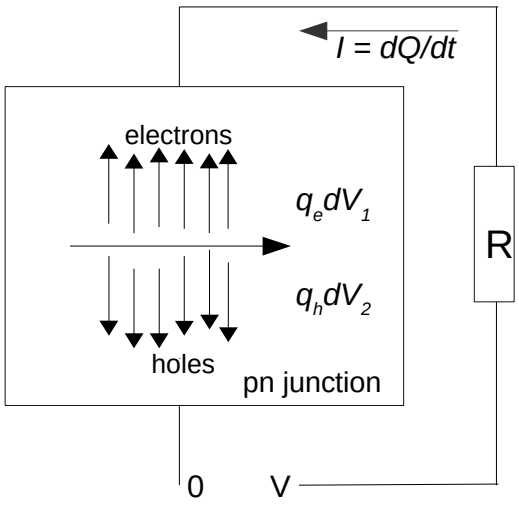

Figure 3.3: Schematics of the working principle of a semiconductor detector. Figure adapted from [23]).

The semiconductor detector is made up of p-type and n-type semiconductor materials, just like a regular semiconductor diode. For nuclear spectroscopy, particularly for determination of the energy of radiation quanta, this detector has become the standard.

A pure germanium crystal placed between two electrodes is almost nonconducting. At room temperature, the electrons in the material are almost entirely valence electrons bound to individual Ge atoms with an energy of 0.75 eV. When such an energy is transferred to a valence electron, it moves to a band of overlapping energy levels that are not associated with a specific atom. In this "conduction band", the electron moves freely through the crystal, indicating that the crystal conducts electricity. Nuclear radiation can provide the energy required to transfer valence electrons to the conduction band.

Since part of the deposited energy is used for crystal excitation, the average energy required to produce an electron-hole pair in germanium at room temperature is 2.9 eV rather than 0.75 eV. A vacancy or "hole" is created when an electron is withdrawn from the valence band. Hence, the ionization process produces an electron-hole pair. The charge through the Ge detector is given by equation:

$$\Delta Q = \frac{e \cdot E_L \cdot \varepsilon}{w}. \tag{3.1}$$

Here, e is electron charge, E_L represents total energy deposited by the particle in the detector, ε is the detector efficiency of collecting the charge, and w denotes the energy required to produce a pair of charge carriers in the detector medium, the constant is the charge of a single charge carrier.

The values of w is 2.95 eV for germanium at 80 K. It is seen that the signal is directly proportional to the energy absorbed in the detector as long as ε is constant. Because w is much smaller in semiconductor detectors than in gas and scintillation detectors, more primary electrons are released in each radiation absorption event, which gives better statistics and thus better energy resolution.

Germanium is much more efficient for radiation detection due to its higher atomic number and due to lower average energy necessary to create an electron-hole pair. Because of the higher atomic number, Ge has a much lager linear attenuation coefficient, which leads to a shorter mean free path. The germanium detectors can have a depleted, sensitive thickness of a few centimeters, and therefore can be used as a total absorption detector for gamma rays up to a few MeV. This makes HPGe detectors particularly well-suited for nuclear spectroscopy [24].

Germanium semiconductor detector made without lithium doping (drifting) is called high purity germanium (HPGe) detector. Continuous cooling is less critical with HPGe detectors; it is not required when storing the crystals, but it should be employed during measuring to increase resolution and avoid crystal overheating due to thermal movement of electrons. HPGe crystals can be either n- or p-type, depending on the type of dominant dopant. Because of the detector capsule wall and insensitive entrance layer, p-type HPGe detectors often have a lower energy cutoff starting at around 100 keV. The relative efficiency of commercially available p-type detectors ranges from 10 to 100 percent. On the other hand, n-type HPGe-detectors can be constructed with a very thin entrance layer and have a lower energy cutoff starting at roughly 6 keV when fitted with a Be-window. In general, n-type HPGe detectors have

lower relative efficiency than p-type detectors, ranging from 10% to 80%. Intrinsic germanium detectors are increasingly replacing lithium-drifted germanium detectors due to their ease of use at a comparable cost and a similar energy resolution [25].

When a large number of photons from the same type of nuclear process interact with the detector crystal, clear patterns form in the a registered pulse height spectrum. The Fig. 3.4 depicts the pulse height spectrum from a measurement with a Co-60 sample. The most pronounced feature of this spectrum is the occurrence of events that form two sharp peaks at specific energies, so-called photo-peaks or full-energy peaks. The area of each peak corresponds to the number of photons at that given energy that interact with the detector via the photoelectric effect.

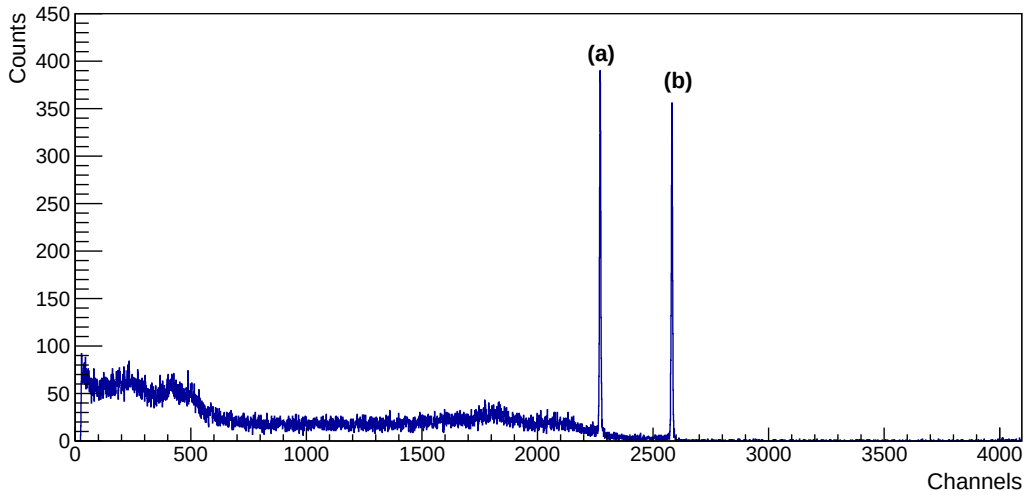

Figure 3.4: ^{60}Co of γ spectra, collected with HPGe detector-III. Here (a) and (b) represent the 1173 and 1332 keV photo-peaks respectively.

In theory, all photons interacting via the photoelectric effect would be sorted into the same channel, resulting in a full-energy peak with a channel width of one. Due to variations in the number of electron-hole pairs created by each interaction, in reality, the full-energy peak shape is close to a Gaussian function. The Full Width at Half Maximum (FWHM) of a full-energy peak is a practical measure of a detector resolution.

Ionizing radiation is present everywhere. Environmental radiations such as radon in indoor air, cosmic radiation, ground, and building materials are

all sources of concern for us. Those external sources contribute background in any spectroscopic measurement, also those of this thesis, aiming at a precise determination of radionuclide content in the examined samples. Energy selectivity along with careful passive shielding of the detectors allowed to suppress the environmental background. When trying to create an effective shield that takes up as little space as possible, a higher attenuation coefficient is preferable. When γ-radiation interacts with the shielding material, vacancies in the atom's inner electron shell can form, resulting in the emission of x-rays once the vacancy is filled. This is known as a material characteristic X-ray radiation, manifesting as peaks in the pulse height spectrum of an HPGe detector. To avoid these effects, the inner layer of the detector shielding could be made of a lighter material that can absorb the characteristic X-rays without self-emitting interrupting X-rays.

3.3.2 Energy calibration

The multichannel analyzer assigns each event to a channel but does not specify the energy to which each event corresponds. Before taking measurements, an energy calibration is required for proper interpretation of a pulse height spectrum.

The gamma energies of certified standard radioactive samples can be used for energy calibration of the spectrum. A linear dependence between the given gamma energy and the position of the corresponding gamma peak in the observed spectrum needs to be determined for this purpose. Fig. 3.4, showing the ^{60}Co spectrum recorded with an HPGe detector, illustrates the procedure, delivering two calibration points: the peak at channel 2271 corresponds to 1173 keV and the peak at channel 2582 is the 1332 keV γ peak.

The calibration sources such as ^{241}Am, ^{133}Ba, ^{109}Cd, ^{60}Co, ^{137}Cs, ^{152}Eu, and ^{22}Na were put on the detector surface, and measurements were taken until good statistics were obtained. After the measurement, the photo-peaks were marked, and the tabulated energy of each peak was assigned. A linear function was fitted to all collected data points:

$$E_\gamma = p_0 + p_1 \cdot C, \tag{3.2}$$

here: E_γ is γ photon energy [keV], p_0 is intercept coefficient [keV], p_1 represents the coefficient of slope [keV/channel] and C is the channel number.

Example of the energy calibration of one of the HPGe detectors used in this study is shown in Fig. 3.5. The valid energy calibration is a prerequisite for a correct identification of the radioisotopes based on their gamma lines.

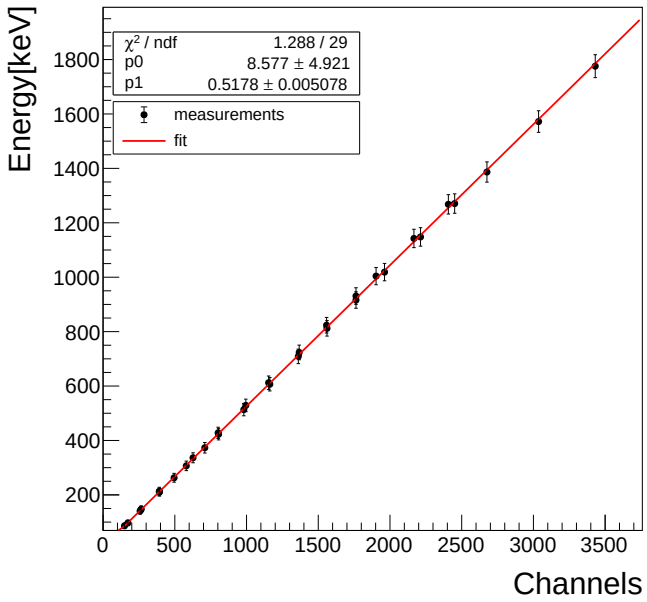

Figure 3.5: Energy calibration curve after the measurements of standard radioactive sources ^{241}Am, ^{133}Ba, ^{109}Cd, ^{60}Co, ^{137}Cs, ^{152}Eu, and ^{22}Na.

3.3.3 Efficiency calibration

The probability that a photon interacts with a detector varies with the photon's energy. The relative efficiency of the detector to register a photon via photo-effect as a function of energy can be determined using standard radioactive calibration sources that produce several photo-peaks at different energies, along with known relative intensities of the different peaks. This is referred to as detector efficiency calibration.

When a γ quanta of E_γ energy is emitted from a radioactive source, it has a certain probability of being fully absorbed by the detector at a given geometry, i.e. the source-detector distance and the detector geometry. This probability is called the efficiency of the detector (ε). To obtain the efficiency,

one needs to register the spectrum of a calibration source of known activity A_{Source}, for a fixed source and detector geometry. After the energy calibration, the spectrum is recorded and the number of counts in each peak (N_{obs}) is obtained by fitting a Gaussian function and removing the linear background. Since the activity of the source and the branching ratio (I_γ) associated with the peak are known, the efficiency is calculated using the following equation:

$$\varepsilon = \frac{N_{obs} \cdot \lambda}{A_{Source} \cdot I_\gamma \cdot (1 - e^{(-\lambda \cdot t_{\text{meas}})})}. \tag{3.3}$$

Here, N_{obs} and I_γ are the number of counts and the branching ratio of the photo-peak, respectively, A_{Source} and λ represent the activity and the decay constant of the calibration source, and t_{irr} is time of measurement.

Fig. 3.6 shows the efficiency calibration measurements at different energies, performed for the ORTEC HPGe detector at the Institute of Physics of the Jagiellonian University. A fit is performed to account for the uncertainties and ensure continuity of the efficiency calibration in gamma energy. In this work, the following fit function is used (for all detectors):

$$ln(\varepsilon) = \sum_{n=0}^{4} a_n (\ln E)^n, \tag{3.4}$$

where a_n are the fitted calibration coefficients.

3.3.4 Gamma-spectroscopy for radioisotope identification

The procedure of detecting a radioisotope's gamma-ray energy is known as gamma-ray spectroscopy (gamma spectroscopy). Gamma-rays can be detected with simple radiation detectors. Gamma-ray spectroscopy, on the other hand, combines a radiation detector with advanced electronics to form an energy spectrometer.The energy spectrometer not only detects but also measures gamma-rays.

Every radioactive material is made up of radioisotopes that emit one or more gamma rays. Each gamma-ray has a distinct and well-defined energy. A gamma-ray database such as [26–28] keeps track of the gamma-ray energies of all radioisotopes. The radioactive material can be identified by measuring the gamma-rays emitted by it and comparing them to a gamma-ray database. Gamma-rays are the radioactive material's unique "fingerprints."

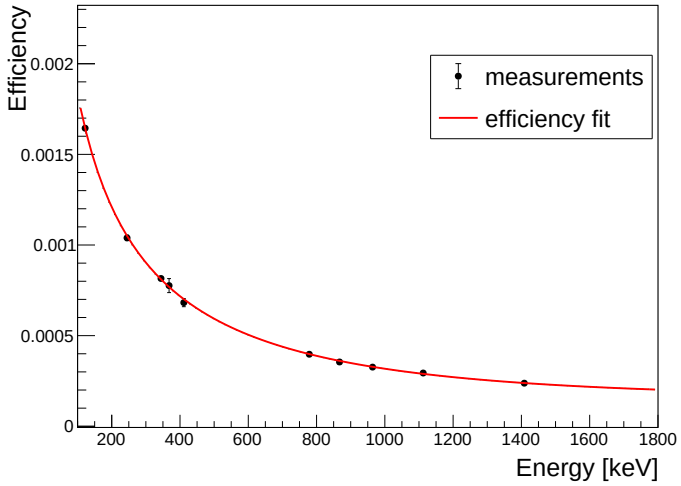

Figure 3.6: Efficiency calibration curve of the Ortec HPGe detector obtained using an ^{152}Eu source located 13 cm above the detector surface.

A simple radionuclide identification is done as discussed in the above paragraph. However, in an advanced analysis, one can determine the quantitative composition of the radioactive sample. To do this, one need to additionally analyse the photopeak areas of the spectrum considering the energy-dependent efficiency of the spectrometer, the gamma emission probability, and activation parameters if necessary.

3.3.5 HPGe detectors in this work

The following HPGe detectors have been used to perform spectroscopic measurements of the irradiated targets:

- HPGe detector constructed at the Institute of Nuclear Physics PAS. Crystal type - p, relative efficiency - 2.5%, energy resolution - 3.4 keV FWHM at the 1332.5 keV peak of ^{60}Co (characterized and operated at the Institute of Nuclear Physics PAS),

- HPGe detector constructed at the Institute of Nuclear Physics PAS. Crystal type - p, relative efficiency - 10%, energy resolution - 3.4 keV FWHM at the 1332.5 keV peak of ^{60}Co (characterized and operated at the Institute of Nuclear Physics PAS),

- HPGe detector manufactured by ORTEC, model: GMX25P4-70, Crystal type - p, relative efficiency - 25%, energy resolution 1.88 keV FWHM at the 1332.5 keV peak of ^{60}Co (characterized and operated at the Institute of Physics, Jagiellonian University).

For simplicity, we named the detectors at the Institute of Nuclear Physics PAS as "detector-I" and "detector-II", and the one used at the Institute of Physics, Jagiellonian University as "detector-III". Although the detector efficiency is larger for small source-detector distance, it is useful to increase that distance in the case of high activity sources to reduce dead time. When operating the detector-I, the distances were varied from 5 cm to 52 cm. That detector was coupled to the SILENA International Multichannel Analyzer mod.8919/PC. For measurements with detector-II, the sources were placed at a distances between 7.45 cm and 28.8 cm and. Signals from that detector were analyzed and acquired using the ORTEC Multichannel Analyzer 919E EtherNIM. For detector-III, two geometries were exploited: a close one where the sample was kept directly on the top of the detector cap and the far one at 13 cm above it. the detector-III signals were fed into the TUKAN 8k Multichannel Analyzer. Analysis of all the acquired data was performed using the ROOT framework (6.10/06 version) .

Detector-I and II were calibrated with ^{241}Am, ^{133}Ba, ^{109}Cd, ^{60}Co, ^{137}Cs, ^{152}Eu, and ^{22}Na calibration sources (both energy and efficiency), whereas detector-III calibration was done using a ^{152}Eu source. Detector-III is shown in Fig. 3.7 as an example of an HPGe detector used in this work. Table. 3.1 gives the nuclear data of the used calibration sources. All detector systems were equipped with low-background lead shielding to reduce the background radiation contribution to the measurement spectra.

Table 3.1: Nuclear data of the calibration sources used in this work (data taken from [26–28]), Uncertainties of the half-life, photon energies and the corresponding intensities in the last valid digits are in italics.

Source	$T_{1/2}$	**Prominent γ lines [keV]**	**Branching ratio (%)**
^{22}Na	2.6019 *4* y	1274.53 *2*	99.944 *14*
^{60}Co	5.2714 *5* y	1173.237 *4*	99.9736 *7*
		1332.501 *5*	99.9856 *4*
^{109}Cd	462.6 *4* d	88.04 *5*	3.61 *10*
^{137}Cs	30.07 *3* y	661.657 *3*	85.1 *2*
^{133}Ba	10.51 *5* y	80.9971 *14*	34.06 *27*
		276.398 *2*	7.164 *22*
		302.853 *1*	18.33 *6*
		356.017 *2*	62.05 *19*
		383.851 *3*	8.94 *3*
^{152}Eu	13.537 *6* y	121.7817 *3*	28.58 *6*
		244.6975 *8*	7.583 *19*
		344.2785 *12*	26.5 *4*
		778.9040 *18*	12.942 *19*
		964.079 *18*	14.605 *21*
		1085.869 *24*	10.207 *21*
		1112.074 *4*	13.644 *21*
		1408.006 *3*	21.005 *24*
^{241}Am	432.2 *7* y	59.5412 *2*	35.9 *4*

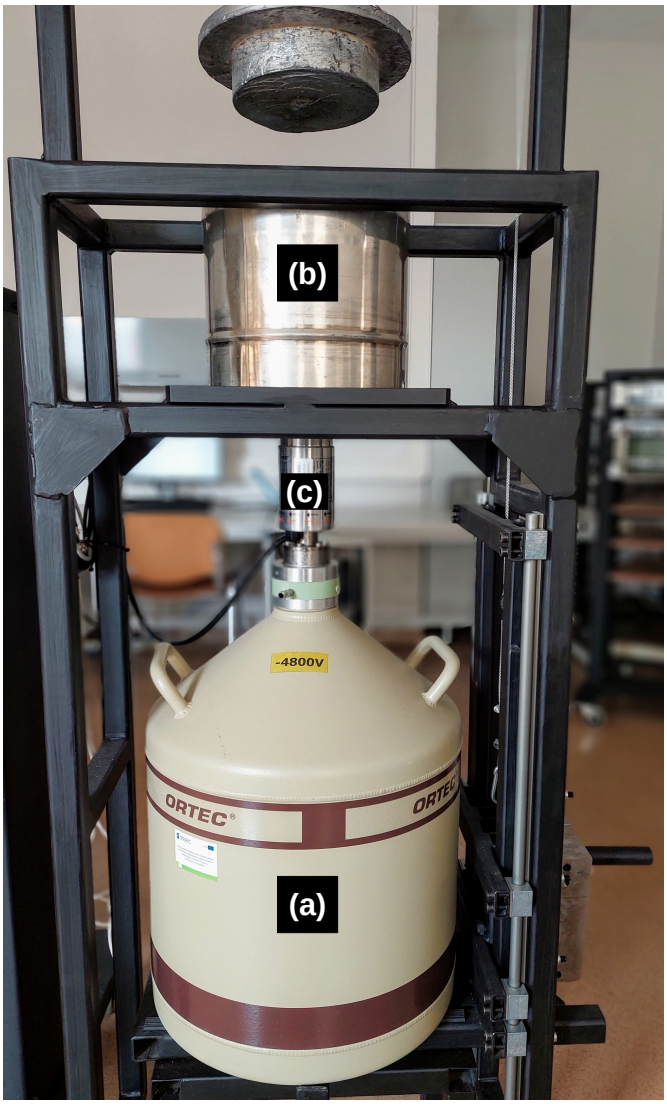

Figure 3.7: ORTEC HPGe detector (detector-III), (a): cryostat with liquid nitrogen, (b): thick lead shielding and (c):HPGe crystal.

Chapter 4

Performed experiments

This chapter presents the performed experiments, setup and data acquisition. ^{nat}Mo is used as a target in both proton and photon irradiation. The isotopic composition of the target is given in Table. 4.1. Targets were 99.9% pure metallic discs of 25 mm diameter and the thickness adjusted for each experiment (will be specified in later sections), and were purchased from Goodfellow Cambridge Limited, UK.

Table 4.1: Isotopic enrichment of ^{nat}Mo target, data taken from [29].

Isotope	Abundance
^{92}Mo	14.53%
^{94}Mo	9.15%
^{95}Mo	15.84%
^{96}Mo	16.67%
^{97}Mo	9.60%
^{98}Mo	24.39%
^{100}Mo	9.82%

4.1 Irradiation with proton beam

In this work, to study the production of ^{99m}Tc/^{99}Mo through (p, x) reactions, we irradiated the ^{nat}Mo targets in two configurations: using a standard single thick target and exploiting the stack-foil activation method.

4.1.1 Single target activation

In this approach, a single 0.5 mm thick ^{nat}Mo disc was irradiated at an external beam line of the AIC-144 cyclotron in the Institute of Nuclear Physics, PAS, Cracow, Poland. As discussed in Sec. 3.1 the cyclotron produces a collimated beam of proton with 60 MeV energy. To reduce the proton energy, a 99% pure aluminum foil of 11.7 mm thickness was used as a degrader. The experimental setup is shown in Fig. 4.1. The Mo target was placed just behind the Al-degrader. The average beam energy at the exit of the degrader was calculated using SRIM [30] and Geant4 simulation software [31]. This value was found to be 26 MeV and energy straggling was 0.16 MeV. Irradiation of the target took place for 5 h and after the end of irradiation the target was left to cool down for 18 h (cooling time, t_c = 18 h). Using SRIM γ-ray attenuation was calculated and the beam spread inside the degrader and the target was studied through Geant4. The size of the proton beam at the entrance position of Al degrader was 5 mm in diameter (measured using a fluorescent sheet).

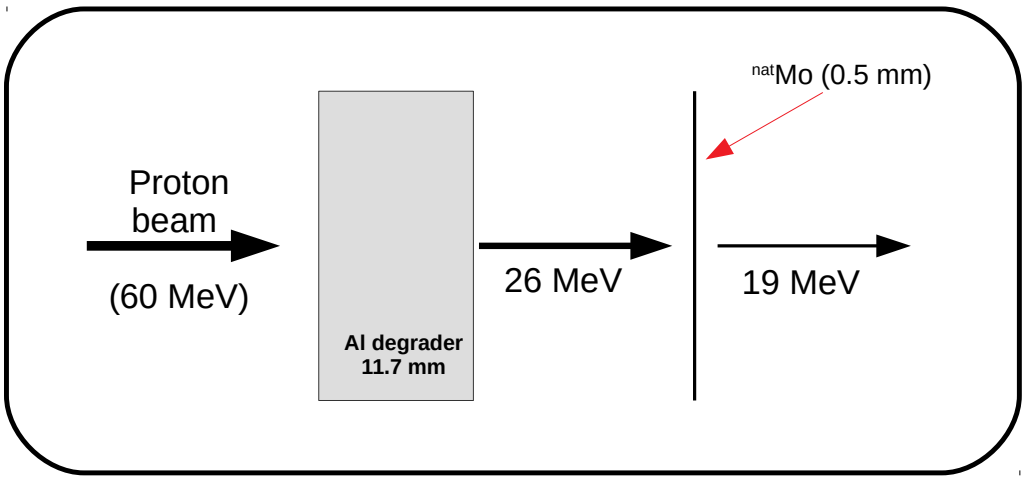

Figure 4.1: Schematics of the single ^{nat}Mo target irradiation setup used at the AIC-144 cyclotron. The ^{nat}Mo target was kept adjacent to the degrader.

The beam diameter changed from 5 mm to 2 cm after passing through the 11.7 mm degrader and at the exit of ^{nat}Mo target beam was 2.3 cm which is less than the diameter of the target. Therefore, the entire beam was incident

on the target. Within the ^{nat}Mo target, the gamma attenuation on average was about 0.5%.

Assuming the incident proton beam energy of 26 MeV on ^{nat}Mo target, the energy loss of beam protons in the target was calculated using SRIM and Geant4. Since the target used in the irradiation was quite thick, the incident energy was degraded by 6.7 MeV. There, the average energy within the target defines the energy scale of all deduced parameters. In this experiment, integrated beam current was determined using the ^{nat}Mo$(p,x)^{m+g96}$Tc monitoring reaction [32].

4.1.2 Stack-foil activation

The experiment was performed using an external beam of AIC-144 cyclotron. To decrease the beam energy to the desired value, a 99.9% pure Al foil of 13.2 mm thickness was used as a degrader. The target setup consisted of 6 metallic discs of ^{nat}Mo of 0.01 mm thickness and 25 mm diameter sandwiched between copper foils (0.01 mm thick). Copper foils were used to monitor the beam current. The stack of targets was irradiated for 5 h and allowed to cool down for 8 h after the end of bombardment. Fig. 4.2 shows the experiment setup. The entire target setup was kept adjacent to each other without any space between the degrader and other target foils.

A fluorescent sheet was placed before the Al-degrader to measure the proton beam dimensions. The diameter of the beam was 5 mm before the degrader and the energy was 60 MeV. Using Geant4 simulations, beam energy distributions on the front and the rear plane of each setup element were calculated. The energy at the end of the degrader was found to be 17.5 MeV with a 0.8 MeV spread and the beam size was 20 mm in diameter.

The beam profile at the end of the target stack was 24 mm broad. Thus, the entire beam profile was contained within the target perimeter. To calculate the beam current throughout the stack, ^{nat}Cu$(p,x)^{62,63,65}$Zn monitoring reactions [32] were used. In this experiment, we have studied proton-induced reactions from 17.3 to 3.3 MeV range. Table. 4.2 shows the experimental conditions during the irradiation in both single and stack-foil setups.

As shown in Fig. 4.2 a thin natural Al-foil (0.02 mm thick) was kept just after the degrader, to stop the ejected heavy product nuclides (recoils) from the preceding targets.

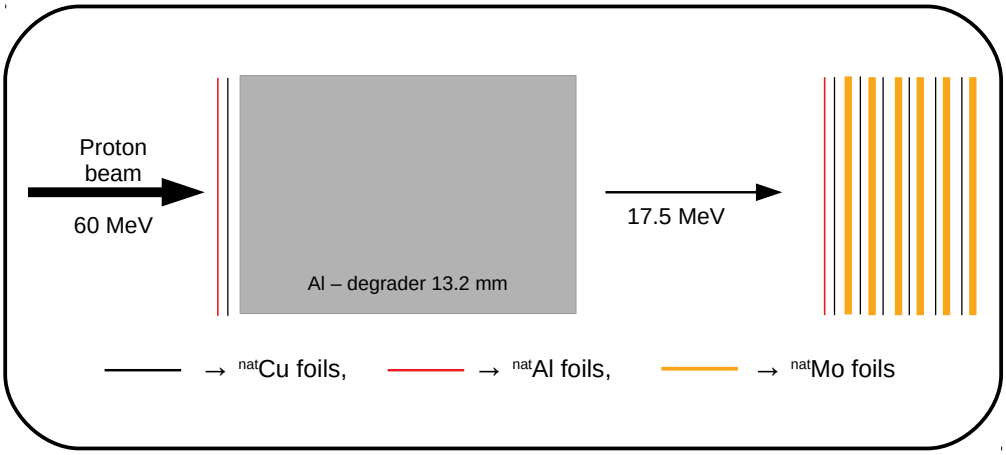

Figure 4.2: Scheme of the stack-foil irradiation setup composed of ^{nat}Mo, ^{nat}Al and ^{nat}Cu targets, irradiated with a proton beam of the AIC-144 cyclotron.The target stack was kept adjacent to Al degrader.

Table 4.2: Experimental conditions of irradiation setup.

Method of target activation	No. of targets irradiated	Degrader thickness [mm]	Beam energy [MeV]	Beam current [nA]	Time of irradiation [h]	Time of cooling [h]
Single	1	11.7	26	28.5	5	18
Stack-foil	6	13.2	17.5	26	5	8

4.2 Irradiation with photon beam

To study the (γ, x) reactions on ^{nat}Mo, experiments were done using 60, 100, 200 MeV electron beam accelerated in the linac injector of the National Synchrotron Radiation Centre SOLARIS, Jagiellonian University, Cracow, Poland. Table. 4.3 lists the beam conditions during the irradiation. In all irradiations, the size of the electron beam spot was 3 mm.

To convert the electron beam into a photon beam, one can take advantage of the bremsstrahlung process. For this purpose, the electron beam was impinged on a natural tungsten brick (99.95% pure) located 26 mm from the linac exit window. The isotopic composition of ^{nat}W brick is given in

Table 4.3: Characteristics of electron beams used in experiments.

Beam energy (MeV)	Repetition frequency (Hz)	Charge of electron bunch (nC)	Average current (e^-/s)	Time of irradiation (h)	Time of cooling (h)
60.0 ± 0.5	10	0.1	0.62×10^{10}	2	2
100.0 ± 0.5	1	1.7	1.06×10^{10}	1	5
200 ± 1	1	1.7	1.06×10^{10}	1	23

Table. 4.4. Tungsten was chosen as a radiator because of its availability and physical properties such as high atomic number and large density, favouring bremsstrahlung production [20]. The lateral dimension of the tungsten radiator was 25 × 25 mm^2 and the thickness was 6 mm. Such a thickness was sufficient to stop the electron beam and was optimized to obtain the highest photon flux, again by means of the Geant4 simulations. A metallic disc of ^{nat}Mo target of 99.9% purity, 0.5 mm thickness and 25 mm diameter was irradiated by placing adjacent to the radiator. The dimension of the ^{nat}Mo target was chosen such that it could encompass the cone of emitted bremsstrahlung radiation. A schematic of the experimental setup is shown in Fig. 4.3.

Table 4.4: Isotopic composition of ^{nat}W radiator.

Isotopes	^{180}W	^{182}W	^{183}W	^{184}W	^{186}W
Abundance (%)	0.12	26.5	14.31	30.64	28.43

4.3 Spectroscopic measurements

4.3.1 Proton-induced reactions

The gamma spectroscopy of radionuclides produced from (p, x) reactions on a single thick ^{nat}Mo target was performed using an energy- and efficiency-calibrated HPGe detector (detector-I, for detector naming see section 3.3.5). The sample was kept 52 cm from the detector window throughout the measurements. The dead time of the detector was monitored and kept below 10%

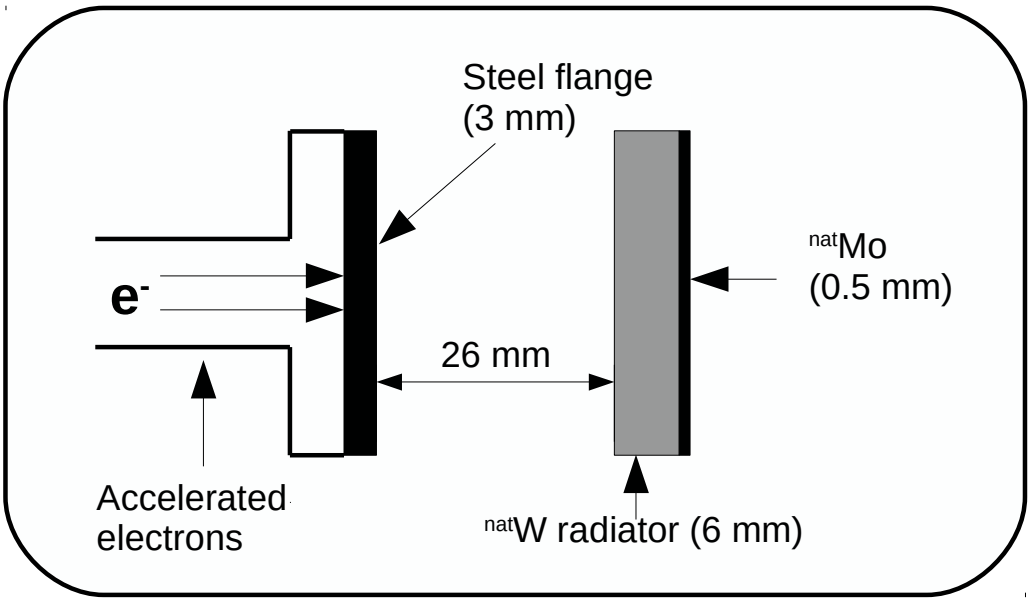

Figure 4.3: Schematic of the experimental setup to study the (γ, x) reactions on $^{\text{nat}}$Mo.

to avoid pile-up effect. To identify the radioisotopes contributing to each photopeak, we conducted a series of sequential measurements, initially in 20 min intervals, then 2 h intervals.

Similarly, to study the activity induced in the target with the stack-foil experiment, the energy and efficiency calibrated detector-II was used. Due to the large activity, and to reduce γ-ray coincidences, five different detector geometries were used in the measurements. The distance between the detector window and the targets varied between 7.45 cm and 28.8 cm. Each target from the stack was examined multiple times at different times after irradiation. A single measurement time varied between 20 min and 5 h and was driven by the counting statistics. Table 4.5 contains the nuclear data of the identified radionuclides adopted from Refs. [26–28]. Fig. 4.4 shows the first registered gamma spectrum from the single target activation experiment.

Table 4.5: Nuclear data for radionuclides produced via proton-induced reactions in a ^{nat}Mo target [26–28]. Gamma ray energies used in the analysis are in bold. Uncertainties of the half-life, photon energies and the corresponding intensities in the last valid digits are in italic.

Radio-nuclide	$t_{1/2}$	E_γ [keV]	I_γ [%]	**Contributing reactions**	**Q-value [MeV]**
^{93}Tc	2.75 h *5*	**1363.02 *4***	**66**	^{92}Mo (p,γ)	4.086
		1477.13 *4*	8.7 *5*	^{94}Mo $(p,2n)$	-13.661
		1520.37 *9*	24.4 *8*	^{95}Mo $(p,3n)$	-21.030
				^{96}Mo $(p,4n)$	-30.185
				^{93m}Tc decay	
^{94}Tc	293 min *1*	449.2 *3*	3.3 *3*	^{94}Mo (p,n)	-5.038
		702.622 *19*	**99.6 *18***	^{95}Mo $(p,2n)$	-12.407
		849.74 *7*	95.7 *18*	^{96}Mo $(p,3n)$	-21.562
		871.09 *18*	100	^{94m}Tc decay	
		916.10 *15*	7.6 *4*		
^{94m}Tc	52.0 min *10*	**871.091 *18***	**94**	^{94}Mo (p,n)	-5.038
		993.19 *9*	2.21 *3*	^{95}Mo $(p,2n)$	-12.407
		1522.11 *20*	4.5 *3*	^{96}Mo $(p,3n)$	-21.562
		1868.68 *8*	5.7 *3*	^{94m}Tc decay	
^{95}Tc	20.0 h *1*	**765.794 *7***	**93.82 *19***	^{94}Mo (p,γ)	4.896
		947.67 *2*	1.951 *19*	^{95}Mo (p,n)	-2.473
		1073.71 *2*	3.74 *4*	^{96}Mo $(p,2n)$	-11.627
				^{97}Mo $(p,3n)$	-18.448
				^{95m}Tc decay	
^{95m}Tc	61 d *2*	**204.117 *2***	**63.25 *13***	^{94}Mo (p,γ)	4.896
		582.082 *3*	29.96 *5*	^{95}Mo (p,n)	-2.473
		835.149 *5*	26.63 *19*	^{96}Mo $(p,2n)$	-11.627
				^{97}Mo $(p,3n)$	-18.448
^{96}Tc	4.28 d *7*	314.337 *71*	2.43 *19*	^{96}Mo (p,n)	-3.756
		778.224 *15*	**99.9**	^{97}Mo $(p,2n)$	-10.577
		812.581 *15*	**82 *4***	^{98}Mo $(p,3n)$	-19.219
		849.929 *13*	98 *4*	^{96m}Tc decay	
		1126.965 *21*	15.2 *12*		
^{99m}Tc	6.01 h *1*	**140.511 *1***	**89**	^{98}Mo (p,γ)	6.500
				^{100}Mo $(p,2n)$	-7.796
				^{99}Mo decay	
^{99}Mo	65.94 h *1*	140.55 *1*	89.43 *23*	^{100}Mo (p,pn)	-8.294
		181.063 *8*	**5.99 *7***		
		366.421 *15*	1.191 *13*		
		739.50 *2*	**12.13 *12***		
		777.92 *20*	4.26 *5*		

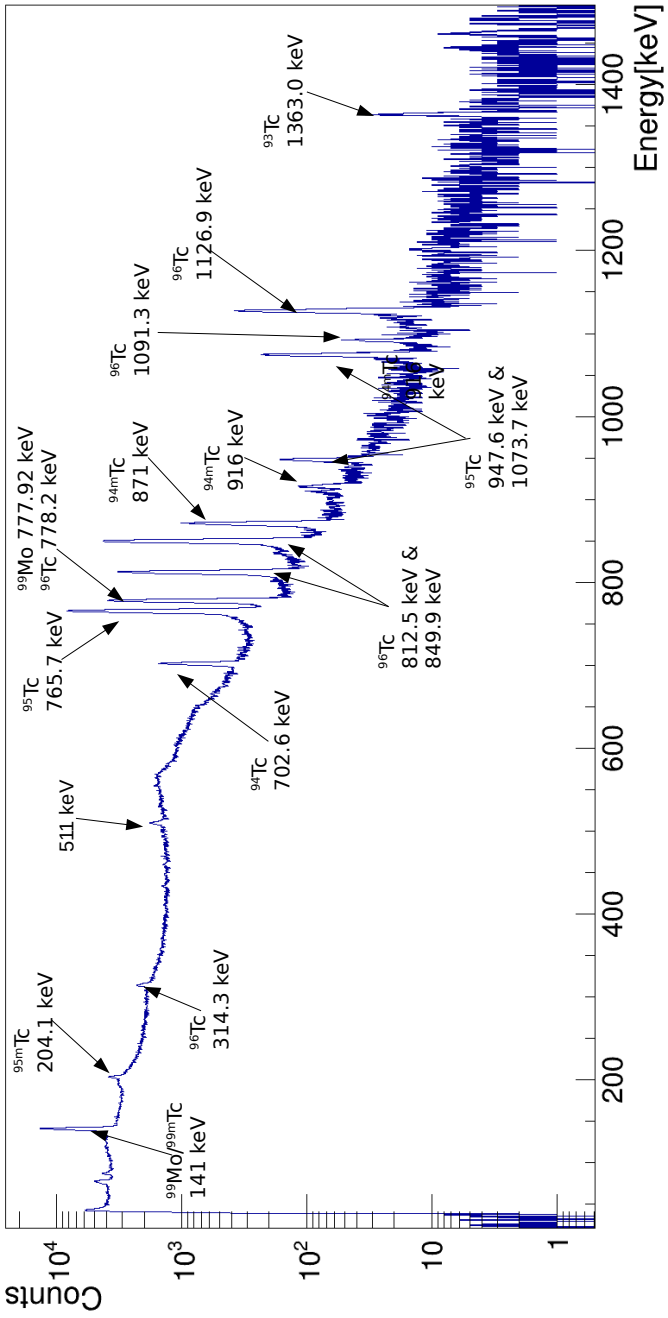

Figure 4.4: Gamma spectrum of ^{nat}Mo target irradiated with 26 MeV proton beam, recorded after 18 hours of cooling time.

4.3.2 Photon-induced reactions

Detector-III, after energy- and efficiency calibration, was used to record the gamma energy spectra from the irradiated target. The dead time of the detector was monitored and kept below 5% to avoid the pile-up effect. Table 4.6 contains the nuclear data of the identified radionuclides. To identify the radioisotopes contributing to each gamma peak, we conducted a series of sequential measurements. For measurements with targets irradiated with the bremsstrahlung of 200 MeV electron beam, we registered the energy spectra of the emitted photons initially in 20-minute intervals, then in 2-hour intervals. For targets irradiated at other beam energies, we proceeded similarly, but with 2-hour measurements only. Fig. 4.5 shows the first registered gamma energy spectrum from the target subjected to the 200 MeV beam irradiation.

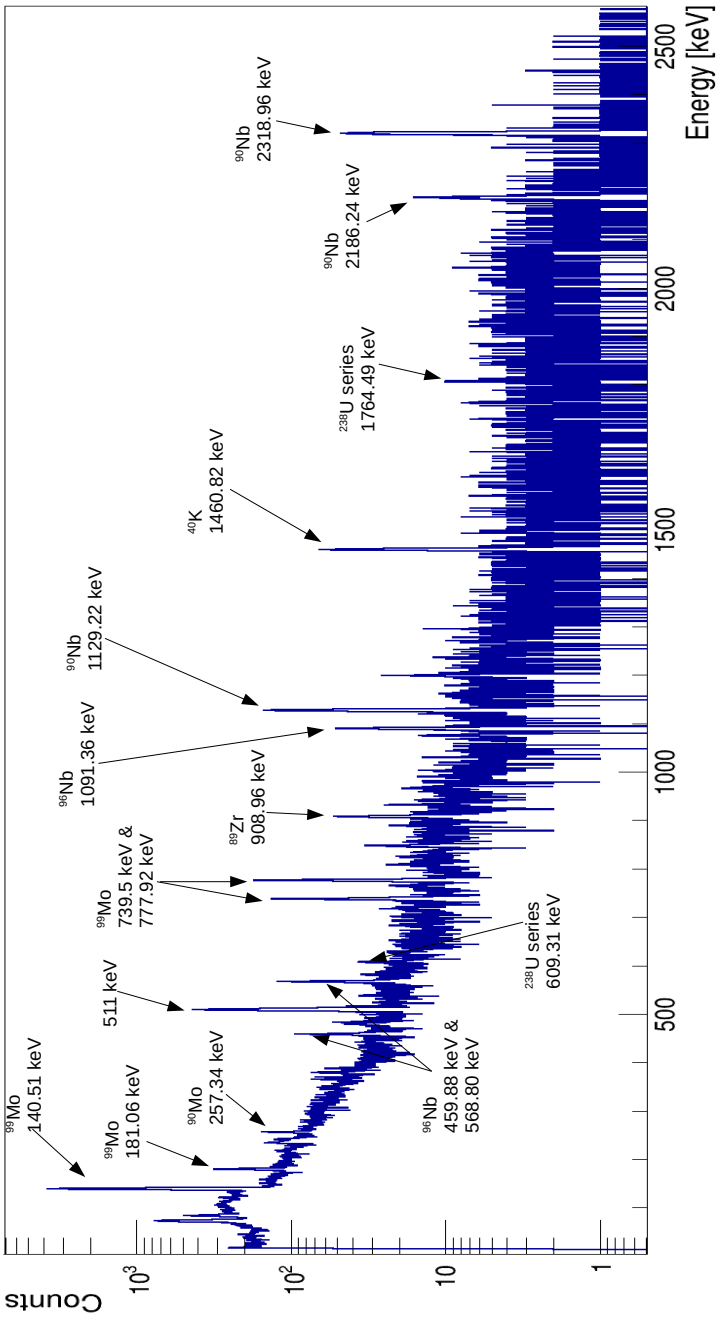

Figure 4.5: Gamma energy spectrum of the $^{\text{nat}}$Mo target irradiated with a 200 MeV photon beam, recorded for 20 min, after 23 hours of cooling time.

Table 4.6: Nuclear data for radionuclides produced by gamma-induced reactions in a ^{nat}Mo target [26–28]. Gamma ray energies used in the analysis are in bold. Uncertainties of the half-life, photon energies and the corresponding intensities in the last valid digits are in italic.

Radionuclide	**Half life ($T_{1/2}$)**	**E_γ [keV]**	**I_γ [%]**	**Contributing reactions**	**Q-value [MeV]**
^{89}Zr	78.41 h *12*	**908.96 *4***	**100**	^{92}Mo $(\gamma, 2pn)$	-24.582
				^{94}Mo $(\gamma, 2p3n)$	-42.330
				^{95}Mo $(\gamma, 2p4n)$	-49.700
				^{96}Mo $(\gamma, 2p5n)$	-58.854
				^{97}Mo $(\gamma, 2p6n)$	-65.675
				^{98}Mo $(\gamma, 2p7n)$	-74.318
				^{100}Mo $(\gamma, 2p9n)$	-88.537
^{90}Nb	14.60 h *5*	141.18 *18*	66.8 *7*	^{92}Mo (γ, pn)	-19.507
		1129.224 *15*	**92.7 *4***	^{94}Mo $(\gamma, p3n)$	-37.255
		1611.76 *3*	2.38 *7*	^{95}Mo $(\gamma, p4n)$	-44.625
		1658.10 *4*	0.335 *15*	^{96}Mo $(\gamma, p5n)$	-53.779
		2186.242 *25*	**17.96 *16***	^{97}Mo $(\gamma, p6n)$	-60.600
		2318.968 *10*	**82.03 *16***	^{98}Mo $(\gamma, p7n)$	-69.243
				^{100}Mo $(\gamma, p7n)$	-83.462
^{92m}Nb	10.15 d *2*	**934.46 *5***	**99**	^{94}Mo (γ, pn)	-17.321
				^{95}Mo $(\gamma, p2n)$	-24.690
				^{96}Mo $(\gamma, p3n)$	-33.844
				^{97}Mo $(\gamma, p4n)$	-40.665
				^{98}Mo $(\gamma, p5n)$	-49.308
				^{100}Mo $(\gamma, p7n)$	-63.528
^{96}Nb	23.35 h *5*	218.98 *13*	2.97 *5*	^{97}Mo (γ, p)	-9.230
		459.88 *12*	**26.62 *19***	^{98}Mo (γ, pn)	-17.873
		568.80 *12*	**58.0 *3***	^{100}Mo $(\gamma, p3n)$	-32.093
		719.562 *14*	6.85 *9*		
		810.8 *2*	**11.09 *10***		
		849.929 *13*	**20.45 *19***		
		1091.34 *12*	0.49 *14*		
^{97}Nb	1.2 h *7*	**658.08 *6***	**98**	^{98}Mo (γ, p)	-9.799
				^{100}Mo $(\gamma, p2n)$	-24.019
^{90}Mo	5.56 h *1*	**257.34 *4***	**78 *8***	^{92}Mo $(\gamma, 2n)$	-22.779
				^{94}Mo $(\gamma, 4n)$	-40.527
				^{95}Mo $(\gamma, 5n)$	-47.896
				^{96}Mo $(\gamma, 6n)$	-57.050
				^{97}Mo $(\gamma, 7n)$	-63.871
				^{98}Mo $(\gamma, 8n)$	-72.514
^{99}Mo	65.94 h *1*	140.55 *1*	89.43 *23*	^{100}Mo (γ, n)	-8.294
		181.063 *8*	**5.99 *7***		
		366.421 *15*	1.191 *13*		
		739.50 *2*	**12.13 *12***		
		777.92 *20*	4.26 *5*		

Chapter 5

Data analysis methods

5.1 Proton-induced reactions

5.1.1 HPGe γ spectroscopy and activity

The procedure of spectroscopic data analysis comprised the following sequence of steps. At first, the HPGe detector was calibrated for energy and efficiency, and then the irradiated targets were examined. Fig. 5.1 shows one of the collected gamma energy spectra from the stack-foil activation experiment. The spectra were normalized by measurement live time. Then, in each spectrum, a region of interest were defined around each of the identified peaks, where a sum of a Gaussian peak and a linear background was fitted (as shown in Fig. 5.2), yielding the peak integral $\dot{n}_{i,j}$. Subsequently, the peak integrals were transformed into the activities at the time of measurement according to the formula

$$A_{i,j} = \frac{\dot{n}_{i,j}}{f_j \epsilon_j \tau_j (1 - e^{-t_{\mathrm{meas},i}/\tau_j})}, \tag{5.1}$$

where the index i runs over the collected spectra at different times after irradiation, j enumerates the identified peaks, τ_j are the mean lifetimes, f_j represents the relative emission probabilities per decay of a parent nucleus, ϵ_j stands for the energy-dependent detector efficiency and $t_{\mathrm{meas},i}$ denotes the duration time of the i-th measurement.

In the next step, for each peak j we constructed a plot of the registered activity versus time after irradiation, and fitted it with an exponential function

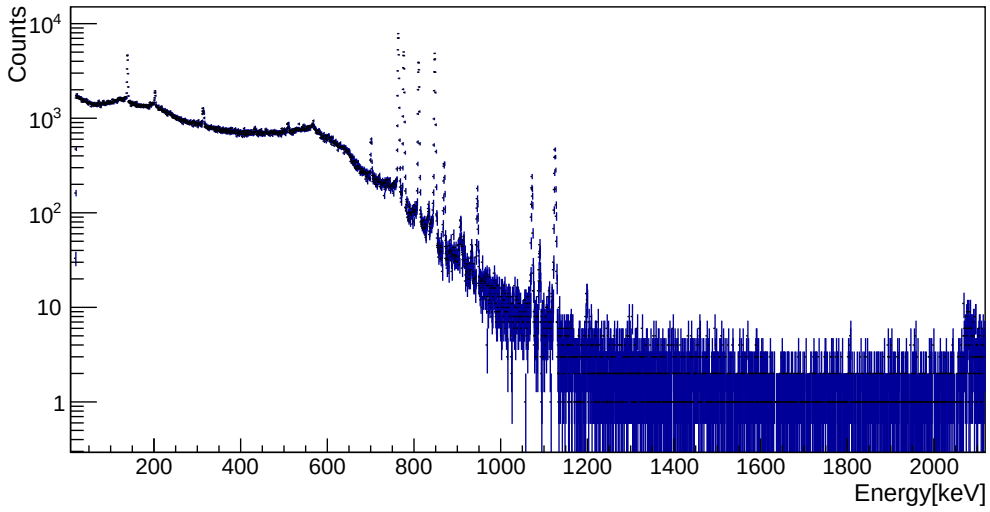

Figure 5.1: Energy-calibrated gamma spectrum from one of the $^{\text{nat}}$Mo targets irradiated in the stack-foil activation experiment.

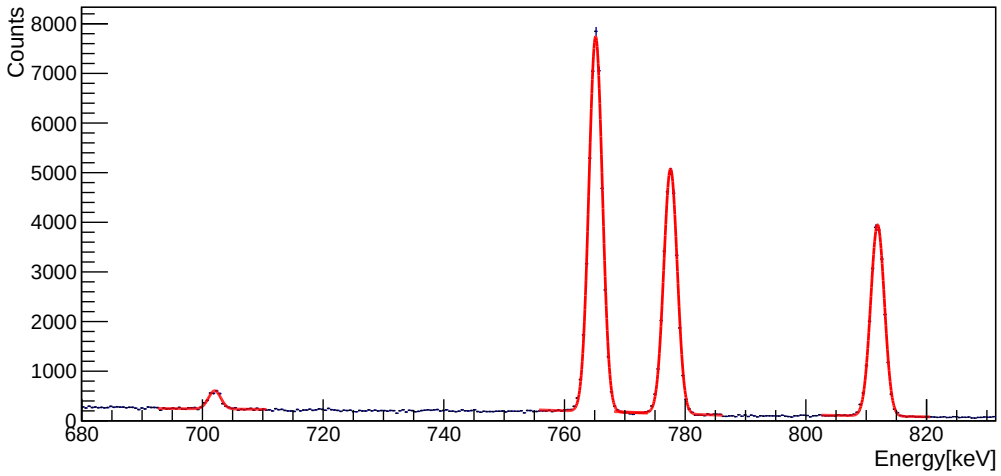

Figure 5.2: Example of photo-peak fitting with a Gaussian function and a linear background, the part of the spectrum is taken from Fig. 5.1.

$$A_j(t) = A_{\text{EOB},j} \exp(-t/\tau_j). \tag{5.2}$$

The τ_j of the function corresponds to the decay time of the radioisotope, and the intercept describes its activity at the end of bombardment. The decay time thus obtained was compared with the literature data, which allowed us to cross-check the identification by peak energy. Fig. 5.3 demonstrates the radioisotope identification process for three different spectral lines. Here we can see that the half-lives of radioisotopes are in agreement with the literature data (Table 4.6) within the 3σ uncertainties for all the identified lines.

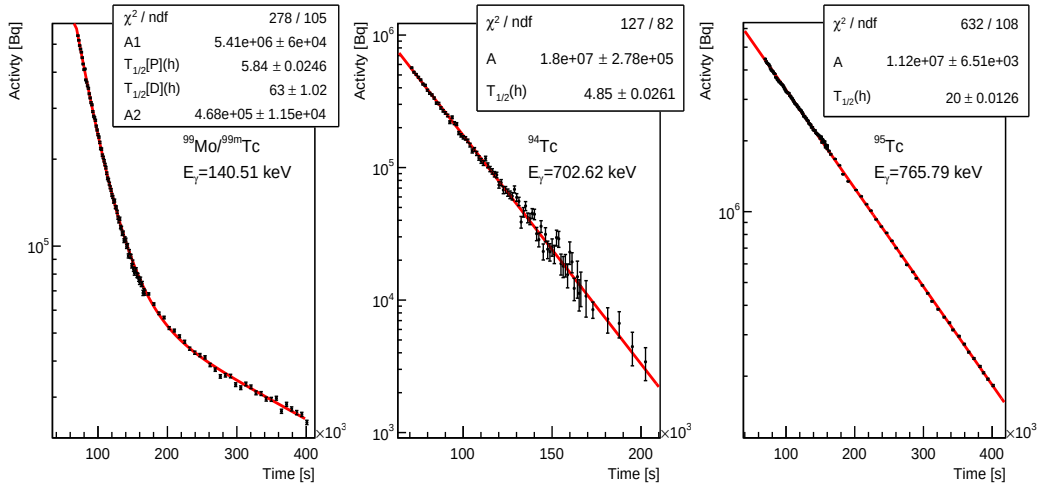

Figure 5.3: Examples of for proton induced reaction: activity versus time dependencies. Red lines represent fitted exponential functions to the data yielding information about the radioisotope activity of the radioisotope at the end of bombardment and its half-life.

Many radionuclides produce gamma lines of the same or nearly the same energy, as discussed in [33–36]. As an example, the radioisomers ^{94}Tc and ^{94m}Tc, emit 871.09 keV gamma quanta. Also the radioisotope pairs ^{94}Tc – ^{94}Nb, ^{95}Tc – ^{95}Nb, and ^{96}Tc –^{96}Nb and many others that decay to the same product, emit gamma of the same energy. The analysis of the 140.51 keV spectral line is the most difficult example in our investigation as it is associated with a decay of ^{90}Nb, ^{99}Mo, and ^{99m}Tc radioisotopes.

In general, to determine the cross section of ^{99m}Tc through direct production, an intense beam with a short irradiation time and cooling period must be used. Both irradiation and cooling time should be less than $\frac{1}{10}$th of the half-life of ^{99m}Tc for accurate estimation [34]. Then the direct production

cross section of ^{99m}Tc can be calculated using the simple standard activation formula. If the above mentioned conditions are not met, necessary modifications to the measured gamma yields must be made, or the standard activation formula must be modified [36]. In the analysis of the single target activation experiment we ignored the contribution of ^{90}Nb since the ^{nat}Mo$(p,x)^{90}$Nb reaction cross section at 19–26 MeV proton energy is insignificant [37]. The standard activation formula was used to find the activity of ^{99}Mo and for ^{99m}Tc, the modified formula described below is used

$$A_{\mathrm{Tc}}(t) = xI\left[\left(\sigma_{\mathrm{Tc}} + P_{\mathrm{Mo}}\frac{\lambda_{\mathrm{Mo}}}{\lambda_{\mathrm{Mo}}-\lambda_{\mathrm{Tc}}}\sigma_{\mathrm{Mo}}\right)(1-e^{-\lambda_{\mathrm{Tc}}t_{irr}})e^{-\lambda_{\mathrm{Tc}}t} - P_{\mathrm{Mo}}\frac{\lambda_{\mathrm{Tc}}}{\lambda_{\mathrm{Mo}}-\lambda_{\mathrm{Tc}}}\sigma_{\mathrm{Mo}}(1-e^{-\lambda_{\mathrm{Mo}}t_{irr}})e^{-\lambda_{\mathrm{Mo}}t}\right] \tag{5.3}$$

here, the subscripts Mo, Tc refer to ^{99}Mo and ^{99m}Tc radioisotopes, $P_{Mo} = 0.876$ is the decay fraction of ^{99}Mo to ^{99m}Tc, and all other terms are the same as previously described.

^{99m}Tc can be produced directly in the reaction ^{nat}Mo$(p,x)^{99m}$Tc and in the decay of ^{99}Mo during the irradiation. Hence the activity of ^{99m}Tc is a sum of two exponential components, as can be seen in Eqn. 5.3, one with a decay constant of ^{99m}Tc and the other with a decay constant of ^{99}Mo. Therefore, to deduce the production cross section of ^{99m}Tc from the yied of the 140.51 keV gamma peak, Eqn. 5.3 was used. All other cross sections were calculated using the standard activation formula (Eqn. 2.19).

For radioisotopes contributing multiple lines to the energy spectrum, the obtained activities were checked to match within 2σ and as a final result a weighted mean was calculated.

5.1.2 Cross section and yield

Substituting the A_{EOB} value from Eqn. 5.2, into the standard activation formula (Eqn. 2.19) and determine the reaction cross section σ [mb]

$$\sigma(E) = \frac{Z\cdot e\cdot M\cdot A_{\mathrm{EOB}}}{H\cdot N_A\cdot\rho\cdot d\cdot I\cdot(1-e^{(-\lambda\cdot t_{irr})})}. \tag{5.4}$$

Here, Z is the atomic number of the projectile, e is the elementary charge, M represents the atomic mass of the target material, H stands for the abundance

of the target, N_A is the Avogadro's number, ρ is the target density [g/cm^3] d is the target thickness [μm], I stands for the beam current [μA], λ denotes the decay constant of the radioisotope [s^{-1}] and t_{irr} represents the irradiation time [s].

If A_{EOB} is induced in thick targets by projectiles of energy E, the experimental value of target yield TY can be obtained from the equations discussed in Sec. 2.2

$$TY(E) = \frac{A_{\mathrm{EOB}}}{I \cdot \tau \cdot (1 - e^{-\lambda \cdot t_{irr}})}. \tag{5.5}$$

5.1.3 Beam intensity

Beam current was determined using the monitoring reactions. From several monitoring reactions (recommended by IAEA [32]), a suitable one should be chosen, with cross-section data in the energy range of the study and the type of projectile employed. In the single target activation using proton beam, $^{\mathrm{nat}}\mathrm{Mo}(p,x)^{m+g96}\mathrm{Tc}$ reaction was used to determine the beam intensity. For the stack-foil activation, $^{\mathrm{nat}}$Cu foils were used as monitoring foils and the corresponding reaction cross-section data was taken from [32]. Copper is an ideal material for a monitoring foil due to its physical, chemical and mechanical properties. Table. 5.1 gives the details of the monitoring foils used in this work along with the lists of the radioisotopes produced in them and used for monitoring. Activity induced in those foils with a well-known reaction cross section, gives the information about the particle flux impinging on the foils. During the preparation of the monitoring foils, special care is taken so that the same area of monitoring foil and production target is exposed to the beam, hence the same particle flux passes through both materials. Monitoring foils were examined in the same manner as the activated target, using the HPGe detectors, then the activities A_{EOB} of the radioisotopes used for monitoring were calculated for each foil.

From Eqn. 2.19 we can calculate the beam intensity based on the obtained activities of the radionuclides used for monitoring A_{EOB} and the literature cross-section value taken at the mean proton energy in the monitoring foil σ_M:

$$I = \frac{A_{\mathrm{EOB}} \cdot M \cdot Z \cdot e}{H \cdot N_A \cdot \sigma_M(E) \cdot \rho \cdot d \cdot (1 - e^{(-\lambda \cdot t_{irr})})}. \tag{5.6}$$

For proton energy ranges for which more than one monitoring reaction was available, the average beam current was calculated. The obtained beam in-

Table 5.1: Details of monitoring foils used in this work and the characteristics of the radioisotopes produced in them and used for beam current determination.

Foil	Thickness [mm]	Product	$T_{1/2}$	γ lines [keV] (intensity)
^{nat}Cu	0.01	^{62}Zn	9.186 h	507.6 (14.8%), 548.35 (15.3%), 596.56 (26%)
		^{63}Zn	38.47 min	669.62 (8.2%), 962.06 (6.5%)
		^{65}Zn	243.96 d	1115.539 (50.04%)
^{nat}Al	0.02	^{24}Na	14.959 h	1368.626 (100%)
^{nat}Mo	0.5	^{96}Tc	4.28 d	778.224 (100%), 812.581 (82%), 849.929 (98%)

tensity was used in further analysis to calculate the cross section σ (Eqn. 5.4) and the target yield TY (Eqn. 5.5).

5.1.4 Beam energy

Monitoring foils can also be used to verify the beam energy irradiating the target [38]. If more than one monitoring radioisotope is produced in the same foil, or by utilizing more than one monitoring foil (of same or different material), then the $A_{\mathrm{EOB},i}$ of each $i-$th radioisotope produced in the foil of thickness x_i and M_i molar mass and with reaction cross section σ_i is measured. Solving Eqn. 2.19 for σ_i, for a pair of the produced radioisotopes ($i = 1, 2$) we can determine the cross-section ratio (r_σ):

$$\underbrace{r_\sigma = \frac{\sigma_1}{\sigma_2}}_{\text{data base}} = \underbrace{\frac{A_{\mathrm{EOB},1}}{A_{\mathrm{EOB},2}} \cdot \frac{M_1 \cdot x_2}{M_2 \cdot x_1} \cdot \frac{1 - e^{(-\lambda_2 \cdot t_{irr})}}{1 - e^{(-\lambda_1 \cdot t_{irr})}}}_{\text{measurements}} . \tag{5.7}$$

The obtained experimental value (right hand side) can be confronted with the $r_\sigma(E)$ calculated based on the recommended cross-section values [32] for each proton energy (or foil). The impinging projectile energy is assumed to be the value where the measured and expected r_σ match. If one uses more than one monitoring foils, then the difference in the energy impinging on the foils should be negligible.

Once the monitoring foils activities were extracted, the cross-section ratio r_σ was calculated for the following pairs: ^{62}Zn/^{63}Zn, ^{62}Zn/^{65}Zn and ^{63}Zn/^{65}Zn and confronted with the expected values based on the reference literature data. This methodology was employed in the stack foil activation experiment.

To verify the above discussed method and to calculate the energy distribution in the target, SRIM and Geant4 simulations were performed. For the single target activation, only simulation values were considered since no monitoring foils were irradiated during the experiment.

Fig. 5.4 shows the proton energy distribution in the subsequent ^{nat}Mo targets (stack-foil activation). The energy distribution in the targets is Gaussian for both proton beams entering and leaving the target. The energy range ΔE in the target is calculated as follows

$$\Delta E = E_{in} + \mathrm{HWHM}(E_{in}) - (E_{out} - \mathrm{HWHM}(E_{out}))\,, \tag{5.8}$$

where E_{in} and E_{out} represent mean proton energies at the front and back plane of the target, respectively, and HWHM(x) stands for the half width at half maximum of the x variable distribution.

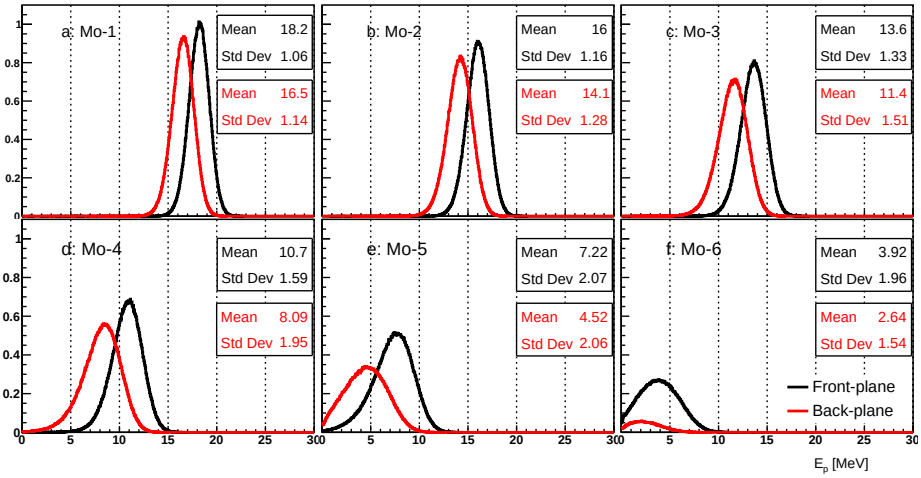

Figure 5.4: Geant4-simulated energy distributions in the subsequent ^{nat}Mo targets, on the front surface (black) and back surface (red) for targets in stack-foil activation experiment.

5.2 Photon-induced reactions

The analysis of spectroscopic data is performed exactly in the same manner as described in the previous section, that is by examination of the activated

targets using an energy and efficiency calibrated HPGe detector. The obtained gamma energy spectra are normalized by the measurement live time. After that, each identified peak was fitted with the sum of a Gaussian and a linear background (as shown in Fig. 5.5). Further, the corresponding radionuclide activity at the end of bombardment was calculated using the peak integral value using Eqn. 5.1.

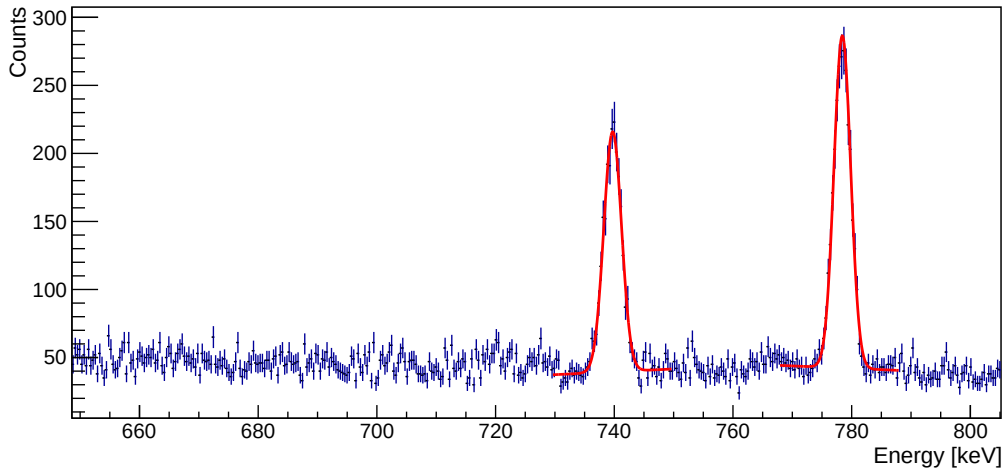

Figure 5.5: A zoom of the gamma energy spectrum collected from a ^{nat}Motarget irradiated with a photon beam of 100 MeV endpoint energy. Fits of Gaussian peaks on linear background used to determine peak integrals needed in the analysis are shown as red lines.

For each identified peak j, the activity-versus-time plots were constructed and the data were fitted with an exponential equation Eqn. 5.2 as shown in Fig. 5.6. The fit yields the value of the decay time of the radioisotope and its activity at the end of bombardment A_{EOB}.

For radioisotopes that contribute more than one photopeak to the spectrum, the obtained activities were checked to ensure that they matched within 2 σ, then a weighted mean was calculated as a final result. To deduce the reaction cross section and production yield, respectively, Eqns. 5.4 and 5.5 were used similarly as for the proton-induced reactions.

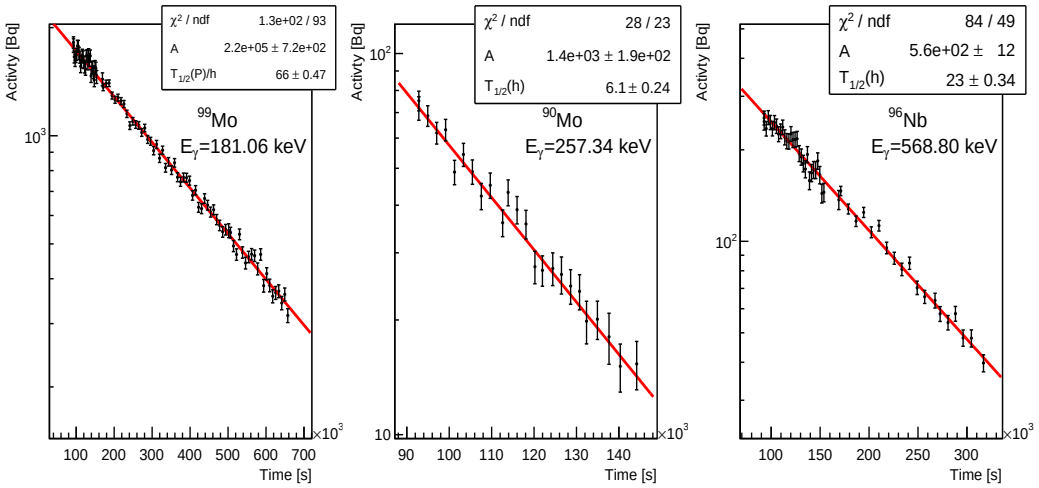

Figure 5.6: Examples of peak identification for the photon-induced reactions: activity versus time dependencies. Red lines represent exponential fits to the data yielding information about the radioisotope activity at the end of bombardment and its half-life.

5.2.1 Beam photon flux

There are no data available for photon-induced monitoring reactions in the energy range of interest. Therefore, to determine the photon flux through the target as a function of energy, Geant4 Monte-Carlo simulations were performed. The resulting number of photons emitted into the forward hemisphere per impinging electron, per cm^2 of radiator area and per 1 MeV of outgoing photon energy range and per second are presented in Fig. 5.7. It is visible that at the higher energy of the electron beam, the bremsstrahlung production is enhanced. The TALYS [39, 40] prediction of the production cross section of ^{99}Mo through the gamma-induced reaction on a ^{nat}Mo target is superimposed in the same figure. The production rate of ^{99}Mocan be calculated as the convolution of the simulated photon flux and the reaction cross section, see Eqn. 2.24.

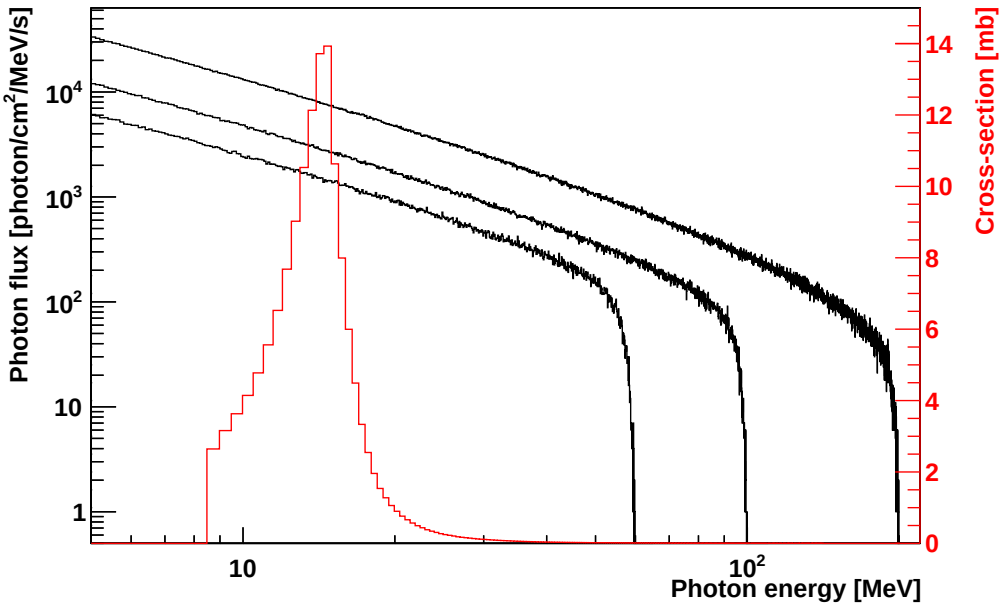

Figure 5.7: Energy spectrum of bremsstrahlung photons emitted into the forward hemisphere generated by 60, 100 and 200 MeV electron beams simulated in Geant4. Total cross section for $^{\mathrm{nat}}\mathrm{Mo}(\gamma, x)^{99}\mathrm{Mo}$ reaction from TALYS prediction is overlaid in red.

Chapter 6

Results and discussion

6.1 Proton-induced reactions

The results of the single and the stack-foil target activation studies are discussed in this section. Results from the single target activation experiment were published in [41] and those from the stack foil experiment were presented in [42]. The cross-section data from both the experiments have been added to the International Atomic Energy Agency (IAEA) database EXFOR [43].

As the proton energy in the single target activation experiment was degraded by nearly 7 MeV in the target, the obtained cross section is in fact averaged over the energy range 19–26 MeV. The ^{nat}Mo$(p,x)^{m+g96}$Tc reaction was used to calculate beam intensity, which was found to be 28.5 ± 3.0 nA. In the stack-foil activation experiment, we have studied proton-induced reactions on ^{nat}Mo target up to 17 MeV, each ^{nat}Mo target in the stack covering a different energy range (Table. 6.1). To determine beam intensity, ^{nat}Cu $(p,x)^{62,63,65}$Zn reactions were exploited and yielded the result of 26.0 ± 1.5 nA.

To compute the cross section, the activation formula of Eqn. 5.4 was used. Table. 6.1 shows the obtained results, as well as the associated uncertainties from both the single and the stack-foil activation experiments. The graphical comparison of the obtained cross sections with the literature data is presented in Fig. 6.1, the literature data were from the EXFOR database [43].

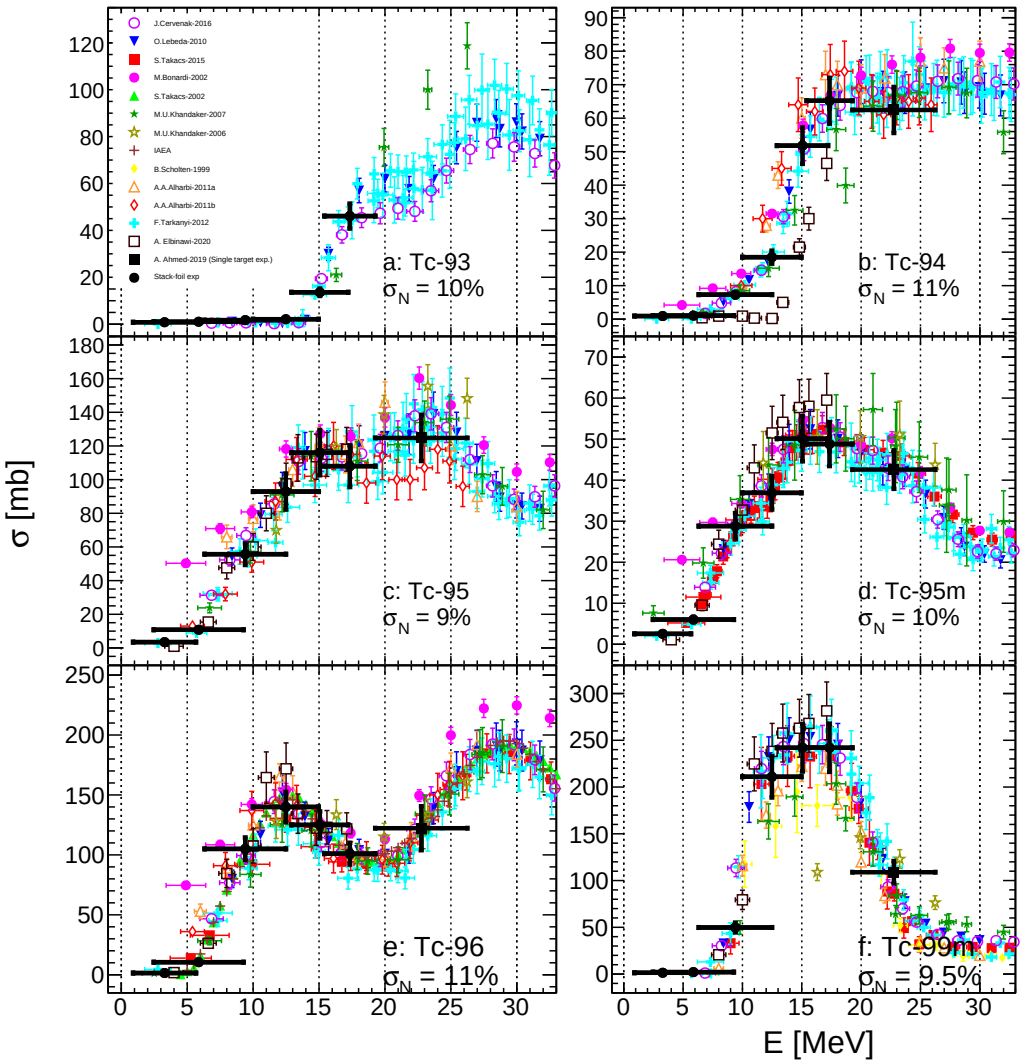

Figure 6.1: Measured production cross sections of $^{\text{nat}}\text{Mo}(p, x)$ reactions from both the single and the stack-foil experiments are presented in black data points (black circles are from the stack-foil experiment and black squares at 22.5 MeV are from the single target experiment) are shown together with other existing literature data sets. Horizontal error bars represent the range of energy degradation within the $^{\text{nat}}$Mo targets (eq. 5.8). The uncertainty of absolute normalization σ_N is stated in each panel.

Table 6.1: Experimentally determined production cross section for all identified radioisotopes in the (p, x) reactions in a ^{nat}Mo target.

Proton	Radionuclide						
energy [MeV]	^{93}Tc	^{94}Tc	^{95}Tc	^{95m}Tc	^{96}Tc	^{99m}Tc	^{99}Mo
3.3 ± 2.7	0.82 ± 0.10	0.92 ± 0.10	3.47 ± 0.42	2.54 ± 0.28	1.45 ± 0.13	1.38 ± 0.15	1.01 ± 0.11
5.9 ± 3.8	1.03 ± 0.12	1.05 ± 0.11	10.8 ± 1.2	6.02 ± 0.66	10.48 ± 0.95	2.09 ± 0.22	1.11 ± 0.12
9.4 ± 3.4	1.71 ± 0.20	7.31 ± 0.77	55.7 ± 6.4	28.8 ± 3.2	104.8 ± 9.6	49.8 ± 5.2	2.16 ± 0.24
12.5 ± 2.7	2.11 ± 0.25	18.5 ± 2.0	93 ± 11	36.9 ± 4.1	140 ± 13	211 ± 22	10.9 ± 1.2
15.1 ± 2.4	13.6 ± 1.6	51.8 ± 5.5	116 ± 14	50.1 ± 5.5	125 ± 12	241 ± 26	34.9 ± 3.9
17.3 ± 2.1	46.1 ± 5.3	65.2 ± 6.9	108 ± 13	48.8 ± 5.4	101 ± 9	242 ± 26	64.8 ± 7.2
22.5 ± 4.8	–	60.1 ± 7.1	120 ± 10	40.4 ± 5.1	120 ± 10	110 ± 10	110 ± 10

6.1.1 Production cross section of ^{99}Mo

The radioisotope ^{99}Mo emits with a large intensity gamma quanta of 140.55 keV [89.43%]. However, this spectral line interferes with the ^{99m}Tc line. To establish the ^{99}Mo production cross section, alternative transitions with lower intensities were used: 181.06 keV ($I_\gamma = 5.99\%$) and 739.5 keV ($I_\gamma = 12.13\%$). Reactions ^{100}Mo$(p, pn)^{99}$Mo and ^{100}Mo$(p, 2p)^{99}$Nb are the production channels that contribute to the production of ^{99}Mo, with ^{99}Nb ($t_{1/2}$= 15 s) decaying to ^{99}Mo via the β-decay. Fig. 6.2 shows a comparison of our obtained cross section with the previously reported data. Since the literature data are reported for enriched ^{100}Mo targets, our data was recalculated to the ^{100}Mo abundance of 97.4% in the target. There is a satisfactory agreement among the data.

6.1.2 Cross section of Tc isotopes production

The reaction which dominates the production of the ^{93}Tc radioisotope ($t_{1/2}$= 2.75 h) is ^{94}Mo(p,2n) [39] and the decay of ^{93m}Tc ($t_{1/2}$= 43.5 min), hence the reported cross section is cumulative. The cross section of ^{93}Tc production was determined using the 1363 keV gamma line of ($I_\gamma = 66\%$). Below 13.8 MeV, the contribution from the ^{92}Mo(p,γ) reaction takes over [39]. The present data are in good agreement with the literature data [33, 35, 44–46], as shown in Fig. 6.1 (a). For beam energy above 19 MeV, the data points in Ref. [44] are significantly above the trend of other data sets. ^{93}Tc was not observed in

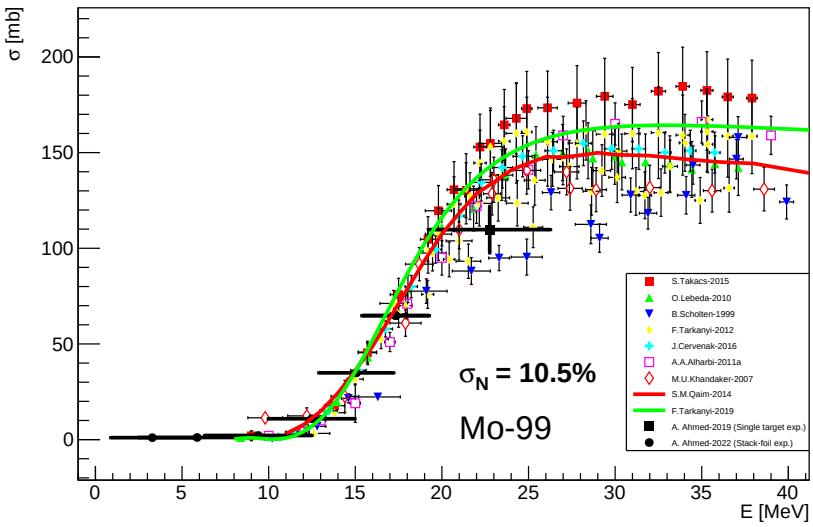

Figure 6.2: Cross section of the ^{100}Mo$(p,x)^{99}$Mo reaction. Black data points represent the results of this thesis, the horizontal error bars cover the range of energy degradation within the $^{\text{nat}}$Mo target (eq. 5.8). The σ_N represents the uncertainty of the absolute normalisation.

the single target experiment because of long cooling time (compared to ^{93}Tc half-life).

The photopeak of the 702.62 keV γ-line (I_γ = 99.6%) was used to determine the production cross section of ^{94}Tc. We primarily evaluated the excitation function of the $^{\text{nat}}$Mo$(p,x)^{94g}$Tc reaction, and the contribution from $^{94\text{m}}$Tc could be ignored because of its short half-life in comparison to the measurement agenda, as described in Ref. [33–36, 41]. The results obtained are in agreement with the literature data, as shown in Fig. 6.1 (b), except of those from Ref. [44], which are for higher beam energies.

The ^{95}Tc radioisotope has a half-life $t_{1/2}$= 20 h. The predominant the decay mode is electron capture. The 765.79 keV (I_γ = 93.82%) gamma line was used to determine the ^{95}Tc activity. The ^{95}Mo(p,n) and ^{96}Mo$(p,2n)$ reactions contribute to the production of ^{95}Tc, with a little contribution from the $^{95\text{m}}$Tc decay. Within the uncertainties, the current results are in good agreement with the literature data from [33, 35, 44–50], as graphically shown in Fig. 6.1 (c).

The long-lived $^{95\text{m}}$Tc isomer is produced the same way as ^{95}Tc. The 204.11 keV γ-line (I_γ = 63.25%) was used to calculate the cross section.

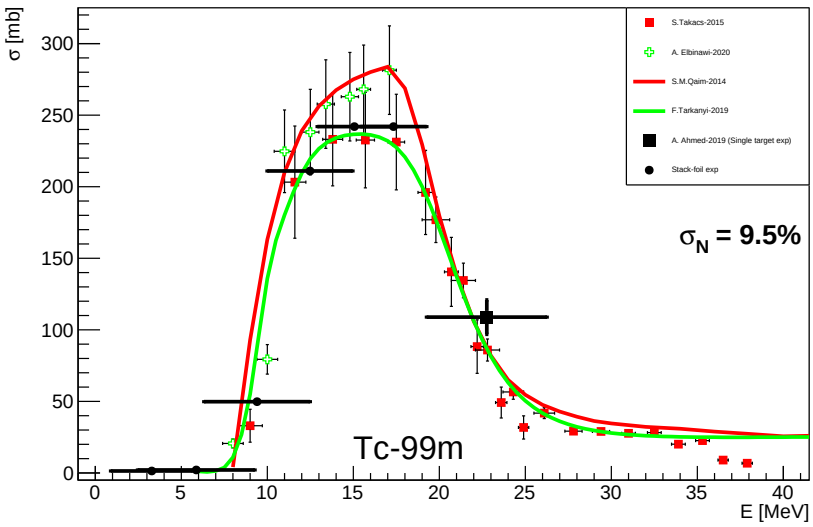

Figure 6.3: Excitation function of the ^{100}Mo$(p,x)^{99m}$Tc reaction. Black points represent the data from this work. Overlaid are the results of theoretical calculations of Ref. [36, 51] represented by red and green curves, respectively, and very recent experimental data from Refs. [34, 46]. The horizontal error bars represent the range of energy degradation within the ^{nat}Mo target (eq. 5.8). The σ_N represents the uncertainty of the absolute normalisation.

For the current proton energy range, the interference of ^{95m}Nb (I_γ = 2.3%) photopeak of the same energy was negligible. The obtained radioisotope production cross section is consistent with existing literature data, as depicted in Fig. 6.1 (d).

The ^{96m}Tc ($t_{1/2}$= 51.5 min) decays to ^{96}Tc (I_γ = 98%) by gamma emission, but the intensity is insufficient for quantitative research [48, 50]. The gamma transitions with energies 778.22 keV (I_γ = 99.9%) and 812.58 keV (I_γ = 82%) were used to calculate the excitation function of ^{96}Tc. We can take the determined cross section as the cumulative cross section of ^{96m}Tc and ^{96g}Tc due to the short $t_{1/2}$ and high isomeric transition decay rate of ^{96m}Tc. The current data is compared to the available database in Fig. 6.1 (e). Our findings are in good agreement with the data that have been published.

While decaying to the ground state, ^{99m}Tc emits only 140.5 keV gamma quanta, which is used in medical applications. The production of ^{99m}Tc radioisotope is dominated by ^{100}Mo$(p,2n)^{99m}$Tc (natural abundance in ^{100}Mo is 9.74%), with a small contribution from the ^{98}Mo$(p,\gamma)^{99m}$Tc process and

Table 6.2: Experimentally determined target yield (TY [MBq/μAh]) of production of all detected radioisotopes through (p, x) reactions in a ^{nat}Mo target from both single and stack-foil experiment.

Proton	Radionuclide						
energy [MeV]	^{93}Tc	^{94}Tc	^{95}Tc	^{95m}Tc	^{96}Tc	^{99m}Tc	^{99}Mo
3.3 ± 2.7	7.02 ± 0.56	1.85 ± 0.16	0.49 ± 0.04	0.011 ± 0.001	0.10 ± 0.01	6.12 ± 0.52	0.36 ± 0.03
5.9 ± 3.8	6.53 ± 0.52	1.96 ± 0.17	0.95 ± 0.09	0.013 ± 0.001	1.10 ± 0.09	7.09 ± 0.60	0.43 ± 0.03
9.4 ± 3.4	9.39 ± 0.75	3.29 ± 0.28	13.8 ± 1.2	0.14 ± 0.01	4.52 ± 0.36	18.1 ± 1.5	0.77 ± 0.06
12.5 ± 2.7	25.9 ± 2.1	28.1 ± 2.4	29.1 ± 2.6	0.18 ± 0.02	8.26 ± 0.66	206 ± 18	2.07 ± 0.17
15.1 ± 2.4	23.6 ± 1.9	61.4 ± 5.2	49.1 ± 4.4	0.26 ± 0.03	10.5 ± 0.8	314 ± 27	5.24 ± 0.42
17.3 ± 2.1	127 ± 10	116 ± 10	57.5 ± 5.2	0.49 ± 0.05	14.8 ± 1.2	418 ± 36	5.42 ± 0.43
22.5 ± 4.8	–	196 ± 16	118 ± 9	0.60 ± 0.05	16.6 ± 1.0	659 ± 53	22.8 ± 1.9

^{99}Mo decay. The 140.5 keV gamma spectral line was used to extract the activity of ^{99m}Tc. This γ-transition was analyzed as described in Ref. [41]. We utilized a ^{nat}Mo target, however the ^{99m}Tc cross section shown here is after extrapolation to 97.4% of ^{100}Mo. The comparison of current and existing literature data is shown in Fig. 6.1 (f). Except for the data of Refs. [44, 48, 52], which show the same trend as the others but smaller cross-section values, there is good agreement with all data sets. In Ref. [36] and more recently in Ref. [51], a theoretical method for modeling the production cross section of ^{99m}Tc and ^{99}Mo was proposed. A comparison of the present data with the relatively recent literature data from Refs. [34, 41, 46] and theoretical calculations of [36, 51] is shown in Fig. 6.3.

6.1.3 Target yield

Table. 6.2 shows the directly determined integral target yields of all investigated radionuclides. Eqn. 5.5 was used to calculate the integral target yield. The target yield is measured in MBq/Ah. The obtained results are plotted as a function of the incident proton energy in Fig. 6.4 (all detected Tc radioisotopes) and Fig. 6.5 (^{99}Mo radioisotope), and they are compared with the literature experimental TY data from [35] and TALYS [39] predictions.

In case of ^{99}Mo and ^{99m}Tc along with [39] prediction and literature data [35], we also compared the results with data from Ref. [34]. It should be noted here, that the TY from TALYS was derived using TALYS cross-section data and not the TALYS produced yield data.

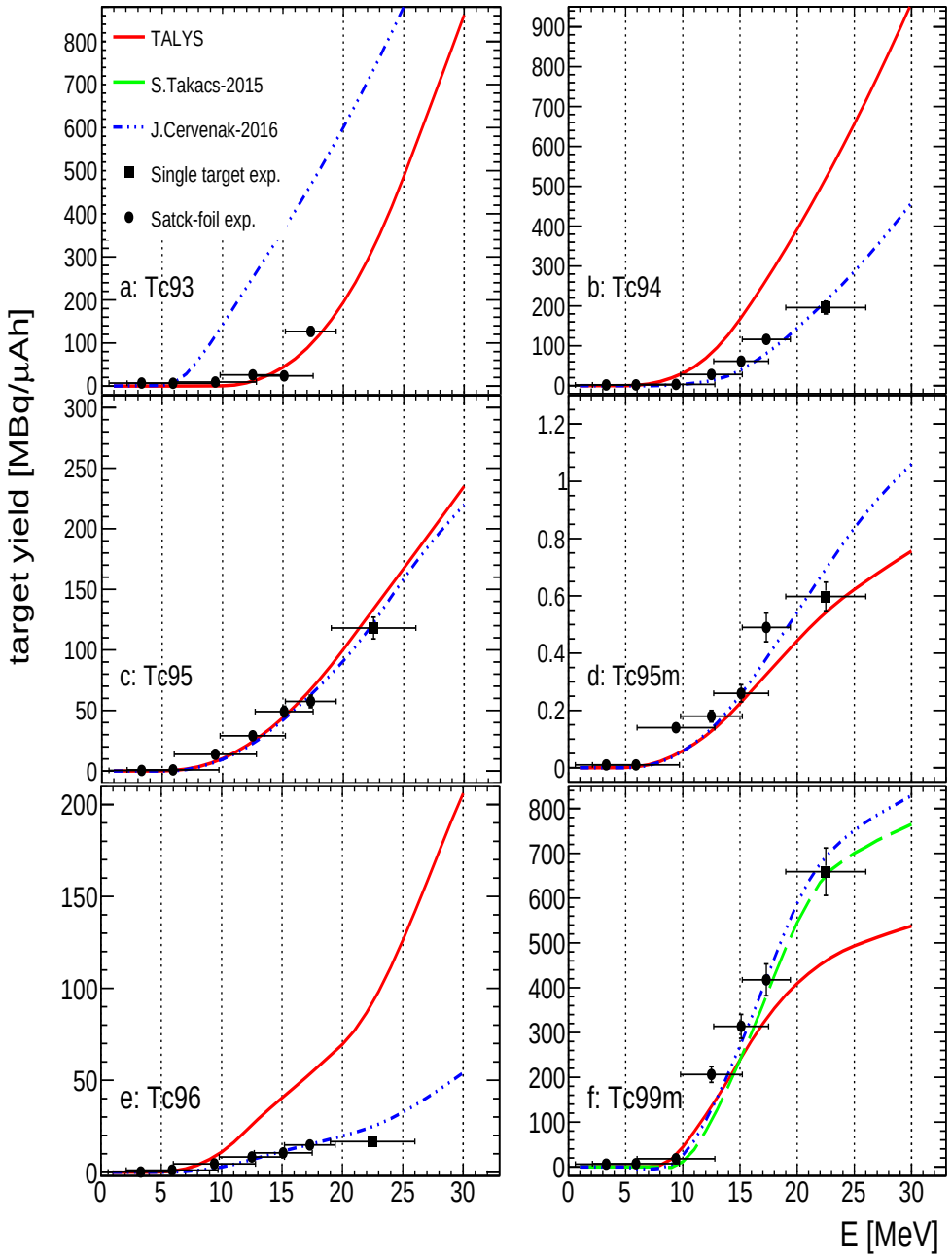

Figure 6.4: Obtained experimental target yield TY for all studied Tc radioisotopes; the long dashed/green and dash-dotted/blue curves reflect the experimental TY from [34] and [35], respectively here the lines represents interpolation of the existing, high-precision data, while the solid/red curve is from TALYS calculations. The error bar here shows the energy range in the target, not the energy uncertainty.

Within the error limitations, the measured integral TY data agrees well with [34], data from [35] is in agreement with our determined TY data except ^{93}Tc as seen in Fig. 6.4 (a) and Fig. 6.5. TALYS predictions overshoot the experimental data for $^{\text{nat}}\text{Mo}(p,x)^{94,96}\text{Tc}$, but in other cases they are in agreement with experimental TY.

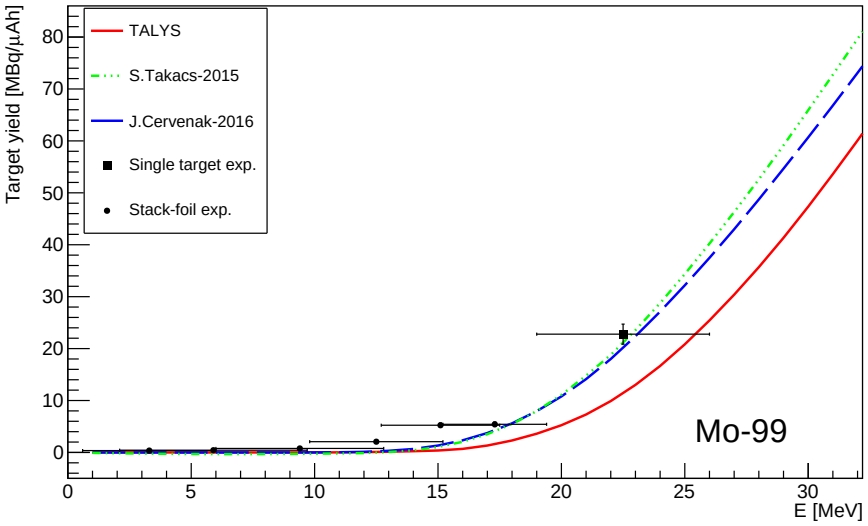

Figure 6.5: Obtained target yield for the $^{\text{nat}}\text{Mo(p,x)}^{99}\text{Mo}$ reaction ; the dash dotted/green and long dashed/blue curves show the experimental TY from [34] and [35], respectively, while the solid/red curve is from TALYS calculations. The horizontal error bars here reflect the energy range in the target, not the energy uncertainty.

6.2 Photon-induced reactions

This section discusses the results from the γ-induced reactions for 60, 100 and 200 MeV end point gamma energies. The results have been published in Ref. [53].

6.2.1 Long-lived impurities produced via $^{nat}Mo(\gamma, x)$ reactions

To estimate the production yield of the long-lived radio-impurities listed in Table. 4.6, we used the Geant4-simulated photon flux convolved with the TALYS package generated cross section of the $^{nat}Mo(\gamma, n)^{99}Mo$ reaction as shown in Fig. 5.7. The scheme discussed in Sec. 2.3 was followed for the calculations. The knowledge of the amount of impurities produced along with the radioisotope of interest is crucial to find the optimal beam conditions for the production as well as to choose an appropriate separation method. Table. 6.3 presents the activity and yield of all studied radioisotopes. The activity is also graphically presented in Fig. 6.6, where the values of ^{99}Mo activity are reduced by a factor of 100. The gamma lines in the spectrum that were used for the determination of A_{EOB} are presented in bold font in Table 4.6. Due to a longer target cooling time for 100 and 200 MeV electron beam irradiation, the short-lived radioisotope ^{97}Nb was not observed, while the induced ^{92m}Nb activity at 60 and 100 MeV was too small to allow conclusive analysis.

Separating therapeutically relevant radionuclides from radioactive contaminants produced in the target can be done by a variety of methods [14]. Only if the specific activity of the radioisotope of interest is high enough, the resulting radio-impurities may be easily removed using a conventional alumina column. However, the separation of ^{99}Mo from ^{90}Mo ($t_{1/2}$= 5.56 h) and other Mo isotopes present in the target is challenging because they are the same chemical element. Thus, instead of the chemical separation, the kinematic recoil approach could be used as discussed in [13]. The low specific activity column approach [54], which is specifically intended to handle such instances, could also be exploited. However, the ideal would be the selection of a set of experimental conditions in which the activity of contaminants is minimal in comparison to the activity of the isotope of interest. The measured ^{99}Mo to ^{90}Mo ratio, which is 25.3 at 60 MeV and is seven times lower than at 100 MeV, similarly at 200 MeV the ratio is found to be 143.7 which is by factor 1.3 lower than at 100 MeV, suggests that energies at around 100 MeV are favorable for ^{99}Mo production with low ^{90}Mo radioisotope contamination.

6.2.2 Production of ^{99}Mo through $^{nat}Mo(\gamma, n)$ reaction

The estimation of the production yield of ^{99}Mo was performed similarly as discussed in Sec. 6.2.1. The experimental activity was determined by

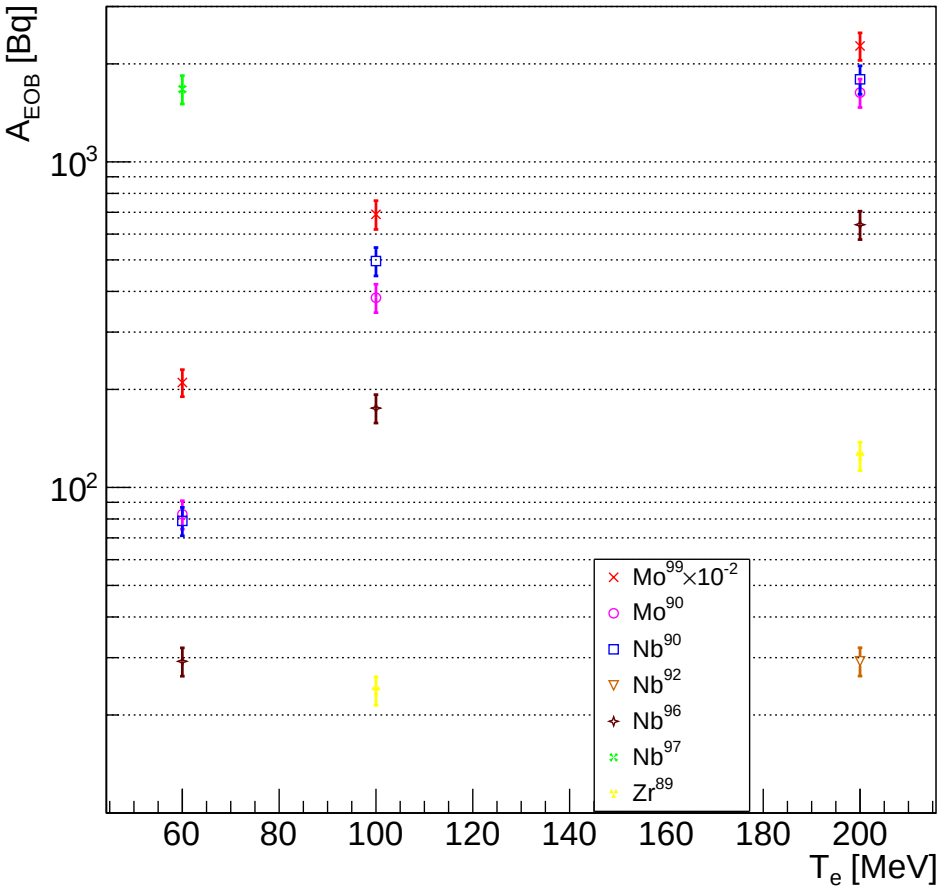

Figure 6.6: Comparison of experimental activity at the end of bombardment (A_{EOB}) for all studied radioisotopes. The results for ^{99}Mo are reduced by 100 for the sake of graphical representation.

analysing the 181 keV and 739.5 keV gamma lines. Although another spectral line of ^{99}Mo at 140 keV is very intense compared to other lines present in the ^{99}Mo spectrum, it overlaps with the 141 keV gamma line of ^{90}Nb hindering its exploitation in the analysis. The resulting ^{99}Mo production rate was found to be 1.5×10^3 s^{-1}, 4.8×10^3 s^{-1} and 21×10^3 s^{-1} for 60, 100 and

Table 6.3: Activity and yield of the produced radioisotopes at the end of bombardment. Columns with values are labelled with the electron beam energy in MeV.

Activity [Bq]			
Radionuclides	**60**	**100**	**200**
^{89}Zr	–	(24±3)	(0.12±0.01)×10^3
^{90}Nb	(79±9)	(0.49±0.05)×10^3	(1.8±0.2)×10^3
^{92m}Nb	–	–	(29 ± 3)
^{96}Nb	(29±2)	(0.17±0.01)×10^3	(0.64±0.05)×10^3
^{97}Nb	(1.7±0.2)×10^3	–	–
^{90}Mo	(83±7)	(0.38±0.03)×10^3	(1.6±0.1)×10^3
^{99}Mo	(2.1±0.2)×10^3	(6.9±0.6)×10^4	(2.3±0.2)×10^5
Yield [Bq/(g·W·h)]			
Radionuclides	**60**	**100**	**200**
^{89}Zr	–	(0.15±0.02)×10^3	(0.77±0.09)×10^3
^{90}Nb	(0.50±0.06)×10^3	(3.1±0.3)×10^3	(11.0±1.2)×10^3
^{92m}Nb	–	–	(0.18±0.02)×10^3
^{96}Nb	(0.18±0.01)×10^3	(1.1±0.1)×10^3	(4.0±0.9)×10^3
^{97}Nb	(14.0±1.4)×10^3	–	–
^{90}Mo	(0.55±0.04)×10^3	(2.5±0.2)×10^3	(11.0±0.9)×10^3
^{99}Mo	(13±1)×10^3	(4.3±0.4)×10^5	(1.4±0.1)×10^6

200 MeV electron beam energy, respectively. The experimental activity and production yield of ^{99}Mo are included in Table. 6.3.

Comparison between the experimentally obtained values and the calculated activity at EOB for all electron beam energies is shown in Table. 6.4. The theoretical predictions overshoot the experimental activity values by about 1.5 times for the 200 MeV beam energy and by about 1.2 times for the two lower beam energies. The predicted yield is also subject to systematic uncertainty, which is difficult to estimate. The calculation is based on the knowledge of cross sections for photonuclear reactions in a very broad energy range. In this work it was calculated using the TALYS package. There are also other approaches to model such processes and calculate their cross sections [55–58]. It is difficult to validate the different libraries with the limited experimental data. For photon end-point energies of 60, 100, and 200 MeV,

Table 6.4: Comparison of ^{99}Mo activity at the end of bombardment obtained from Geant4 + TALYS prediction and from experimental data.

Beam energy (MeV)	$\mathbf{A_{EOB}}$ **Geant4 + TALYS [MBq]**	$\mathbf{A_{EOB}}$ **Experimental [MBq]**
60	0.025	0.021± 0.002
100	0.081	0.069± 0.007
200	0.34	0.23± 0.03

respectively, the disparities are 2σ, 2σ and 3σ, where σ signifies the relevant statistical uncertainty in each case. Given the unknown systematic uncertainties, our results are consistent with the TALYS + Geant predictions.

Chapter 7

Summary and outlook

This thesis presents possible production routes of ^{99}Mo/^{99m}Tc medical radioisotope generator with the use of accelerators through proton- and photon-induced reactions on ^{nat}Mo targets. For proton induced reactions excitation functions and target yields data were obtained experimentally for the production of the above-mentioned radioisotopes and other radioactive contaminants produced in the target.

The proton-induced reactions were studied through two methods, i.e., Single thick target activation (19-26 MeV) and stack-foil activation (0-17 MeV). The results from proton-induced experiments were also compared with other reported literature data. The gamma-induced reactions were studied using 60, 100 and 200 MeV end point bremsstrahlung energies. The results from 100 and 200 MeV are the world first experimental reported data. The experimental results were used to estimate the conditions for the large-scale production optimized to suppress impurities.

The findings of this study provide useful information about the accessibility of the analyzed radioisotopes for research on the next necessary steps, such as chemical separation and recovery of the target material, labelling of biologically active molecules, and in vitro and in vivo experiments (biodistribution, imaging quality or therapeutic effect), preclinical and clinical studies. The ultimate goal in this march is the efficient production of effective radiopharmaceuticals using ^{nat}Mo targets.

The price of enriched Mo is currently around $30,000 per gram, whereas the price of ^{nat}Mo ranges from $0.25 to $0.80 per gram [59]. By increasing the irradiation period and employing natural molybdenum targets, one can lower the cost while still achieving the desired yield. Impurity formation can be

reduced by using protons with the energy of 9–26 MeV. It was demonstrated that the use of ^{nat}Mo target could provide a very pure ^{99}Mo source for ^{99m}Tc extraction by using traditional procedures [47, 60].

Our research indicates that the existing electron linacs are a viable and interesting alternative to low-energy or dedicated facilities for the production of ^{99}Mo. The beam lifetime in the ring of synchrotrons is of the order of several hours, and linac injectors are only used for a small part of that period. At those facilities, ^{99}Mo could be produced in a parasitic manner, in parallel with other ongoing experiments. It would lead to a more efficient use of the existing infrastructure while meeting the local demand for ^{99}Mo, thereby eliminating losses that are unavoidable in transportation. One could still use the enriched Mo target to increase the yield and reduce the production of radioimpurities. In case of photon-induced reactions, the yield could be further increased by opting much thicker targets at higher beam energies, taking advantage of electromagnetic cascades created by high-energy photons, in which the secondary photons carry sufficient energy to induce photonuclear reactions.

More than 50 electron linac facilities, similar to SOLARIS, exist in research institutes all over the world, delivering beams of energy more than 100 MeV. 22 of them are located in Europe [61, 62], and many of them deliver beam currents several times higher than SOLARIS. Those facilities can be used to find optimal beam conditions for the ^{99}Mo production via photonuclear reactions, leading to the development of standardized production procedures for commercial applications. This kind of investigation has also the potential to be extended to other radioisotopes relevant for medicine or industry.

Bibliography

[1] *Radioisotopes in Medicine. World Nuclear Association.* https://www.world-nuclear.org/information-library/non-power-nuclear-applications/radioisotopes-research.aspx.

[2] *Radiology info for patients- General nuclear medicine*, https://www.radiologyinfo.org/en/info/gennuclear.

[3] *Nuclear Medicine*, https://www.nibib.nih.gov/science-education/science-topics/nuclear-medicine.

[4] *Kuhl and Edwards Produce CT Scan*, https://ethw.org/Kuhl_%26_Edwards_Produce_CT_Scan.

[5] I. Rausch, F. G. Füchsel, C. Kuderer, M. Hentschel, and T. Beyer, "Radiation exposure levels of routine SPECT/CT imaging protocols", European Journal of Radiology **85**, 1627–1636 (2016) https://doi.org/10.1016/j.ejrad.2016.06.022.

[6] *Basic principle of SPECT*, https://www.lbic.lu.se/basic-principles-petct-and-spectct.

[7] T. Sharir, P. J. Slomka, and D. S. Berman, "Solid-State SPECT technology: fast and furious", Journal of Nuclear Cardiology **17**, 890–896 (2010) https://doi.org/10.1007/s12350-010-9284-5.

[8] Nuclar Energy Agency, *Medical radiosotopes*, https://www.oecd-nea.org/med-radio/.

[9] R. Crasta, H. Naik, S. V. Suryanarayana, P. M. Prajapati, K. C. Jagadisan, S. V. Thakare, S. Ganesh, V. T. Nimje, K. C. Mittal, and A. Goswami, "Photo-neutron cross-section of ^{100}Mo", Journal of Radioanalytical and Nuclear Chemistry **290**, 367–373 (2011) https://doi.org/10.1007/s10967-011-1247-z.

[10] Yu. D. Tur, "Linear electron accelerator for the medical isotopes production", in Proceeding of EPAC, Vienna, Austria (2000), pp. 2560–2562.

[11] T. J. Ruth, "A short term solution to the medical isotope crisis via direct production of Tc-99m at low energy: A piece of the puzzle", La Physique AU Canada **66**, 15–16 (2010).

[12] C. Brown, "Will new isotope sources be ready in time?", Canadian Medical Association Journal **188**, 252–252 (2016) https://doi.org/10.1503/cmaj.109-5224.

[13] V. N. Starovoitova, L. Tchelidze, and D. P. Wells, "Production of medical radioisotopes with linear accelerators", Applied Radiation and Isotopes **85**, 39–44 (2014) https://doi.org/10.1016/j.apradiso.2013.11.122.

[14] S. M. Qaim, "Cyclotron production of medical radionuclides", in *Handbook of nuclear chemistry* (Springer US, Boston, MA, 2011), pp. 1903–1933, https://doi.org/10.1007/978-1-4419-0720-2_39.

[15] N.I. Aizatsky and N.P. Diky and A.N. Dovbnya and D.Ehst1 and Yu.V. Lyashko and V.I. Nikiforov and A.Eh. Tenishev and A.V. Torgovkin and V.L. Uvarov and V.A. Shevchenko and B.I. Shramenko, "^{99}Mo and ^{67}Cu isotope yields under production conditions of NSC KIPT electron accelerator KUT-30", Problems of Atomic Science and Technology **53**, 140–144 (2010).

[16] V. N. Starovoitova, P. L. Cole, and T. L. Grimm, "Accelerator-based photoproduction of promising beta-emitters ^{67}Cu and ^{47}Sc", Journal of Radioanalytical and Nuclear Chemistry **305**, 127–132 (2015) 10.1007/s10967-015-4039-z.

[17] D. Rotsch, K. Alford, J. Bailey, D. Bowers, T. Brossard, M. Brown, S. Chemerisov, D. Ehst, J. Greene, R. Gromov, J. Grudzinski, L. Hafenrichter, A. Hebden, T. Heltemes, W. Henning, J. Jerden, C. Jonah, M. Kalensky, J. Krebs, V. Makarashvili, B. Micklich, J. Nolen, K. Quigley, J. Schneider, N. Smith, D. Stepinski, P. Tkac, G. Vandegrift, M. Virgo, K. Wesolowski, and A. Youker, "Production of Medical Isotopes With Electron Linacs", in Proc. of North American Particle Accelerator Conference (NAPAC 16), Chicago, IL, USA, October 9-14, 2016, North American Particle Accelerator Conference 3 (2017), pp. 1091–1095, https://doi.org/10.18429/JACoW-NAPAC2016-THB2IO02.

[18] Ralph G. Bennett and Jerry D. Christian and David A. Petti and William K. Terry and S. Blaine Grover, "A System of 99m-Tc Production Based on Distributed Electron Accelerators and Thermal Separation", Nuclear Technology **126**, 102–121 (1999) https://doi.org/10.13182/NT99-A2961.

[19] A. Gopalakrishna, H. Naik, S. V. Suryanarayana, Y. Naik, V. T. Nimje, B. K. Nayak, S. K. Sarkar, S. Padmanabhan, C. Kothalkar, P. Naskar, A. C. Dey, and A. Goswami, "Preparation of ^{99}Mo from the ^{100}Mo(γ, n) reaction and chemical separation of ^{99m}Tc", Journal of Radioanalytical and Nuclear Chemistry **308**, 431–438 (2016) https://doi.org/10.1007/s10967-015-4481-y.

[20] H. Naik, S. V. Suryanarayana, K. C. Jagadeesan, S. V. Thakare, P. V. Joshi, V. T. Nimje, K. C. Mittal, A. Goswami, V. Venugopal, and S. Kailas, "An alternative route for the preparation of the medical isotope ^{99}Mo from the ^{238}U(γ, f) and ^{100}Mo(γ, n) reactions", Journal of Radioanalytical and Nuclear Chemistry **295**, 807–816 (2013) https://doi.org/10.1007/s10967-012-1958-9.

[21] H. Naik, G. N. Kim, R. Kapote Noy, R. Schwengner, K. Kim, M. Zaman, S. G. Shin, Y. Gey, R. Massarczyk, R. John, A. Junghans, A. Wagner, and M. H. Cho, "Photo-neutron reaction cross-sections for ^{nat}Mo in the bremsstrahlung end-point energies of 12-16 and 45-70 MeV", The European Physical Journal A **52**, 1–14 (2016) https://doi.org/10.1140/epja/i2016-16195-9.

[22] E. W. Phelan, *Radioisotopes in Medicine*, Understanding The Atom (United States Atomic Energy Commission, United States of America, 1967).

[23] *Nuclear medicine physics*, Non-serial Publications (INTERNATIONAL ATOMIC ENERGY AGENCY, Vienna, 2015).

[24] *Principle of Operation of HPGe Detectors*, https://www.nuclear-power.com/nuclear-engineering/radiation-detection/semiconductor-detectors/high-purity-germanium-detectors-hpge/principle-of-operation-of-hpge-detectors/.

[25] G. Choppin, J.-O. Liljenzin, J. Rydberg, and C. Ekberg, "Chapter 9 - detection and measurement techniques", in *Radiochemistry and nuclear chemistry (fourth edition)*, edited by G. Choppin, J. O. Liljenzin,

J. Rydberg, and C. Ekberg, Fourth Edition (Academic Press, Oxford, 2013), pp. 239–295, https://doi.org/10.1016/B978-0-12-405897-2.00009-4.

[26] *Nuclear structure and decay data*, https://www-nds.iaea.org/relnsd/vcharthtml/VChartHTML.html.

[27] *National Nuclear Data Center, Brookhaven National Laboratory*, https://www.nndc.bnl.gov/.

[28] S.Y.F. Chu and L.P. Ekström and R.B. Firestone, "Table of Radioisotopes Version 2.0", The Lund/LBNL Nuclear Data Search, http://nucleardata.nuclear.lu.se/toi/index.asp.

[29] *Nuclear structure and decay data Nudat 2.8*, https://www.nndc.bnl.gov/nudat2/indx_sigma.jsp, 2019.

[30] J. F. Ziegler, J. P. Biersack, and M. D. Ziegler, "SRIM code, version 2013", (2013).

[31] *Geant4 (simulation software) Version 10.2.3, 2017*, http://geant4.web.cern.ch/geant4/index.shtml.

[32] A. Hermanne, A. Ignatyuk, R. Capote, B. Carlson, J. Engle, M. Kellett, T. Kibédi, G. Kim, F. Kondev, M. Hussain, O. Lebeda, A. Luca, Y. Nagai, H. Naik, A. Nichols, F. Nortier, S. Suryanarayana, S. Takács, F. Tárkányi, and M. Verpelli, "Reference Cross Sections for Charged-particle Monitor Reactions", Nuclear Data Sheets **148**, 338–382 (2018) https://doi.org/10.1016/j.nds.2018.02.009.

[33] O. Lebeda and M. Pruszyński, "New measurement of excitation functions for (p,x) reactions on ^{nat}Mo with special regard to the formation of ^{95m}Tc, $^{96m+g}$Tc, ^{99m}Tc and ^{99}Mo", Applied Radiation and Isotopes **68**, 2355–2365 (2010) https://doi.org/10.1016/j.apradiso.2010.05.011.

[34] S. Takács, A. Hermanne, F. Ditrói, F. Tárkányi, and M. Aikawa, "Reexamination of cross sections of the ^{100}Mo$(p,2n)^{99m}$Tc reaction", Nuclear Instruments and Methods in Physics Research Section B: Beam Interactions with Materials and Atoms **347**, 26–38 (2015) https://doi.org/10.1016/j.nimb.2015.01.056.

[35] J. Červenák and O. Lebeda, "Experimental cross-sections for proton-induced nuclear reactions on ^{nat}Mo", Nuclear Instruments and Methods in Physics Research Section B: Beam Interactions with Materials and Atoms **380**, 32–49 (2016) https://doi.org/10.1016/j.nimb.2016.05.006.

[36] S. Qaim, S. Sudár, B. Scholten, A. Koning, and H. Coenen, "Evaluation of excitation functions of ^{100}Mo(p,d+pn)^{99}Mo and ^{100}Mo(p,2n)^{99m}Tc reactions: Estimation of long-lived Tc-impurity and its implication on the specific activity of cyclotron-produced ^{99m}Tc", Applied Radiation and Isotopes **85**, 101–113 (2014) https://doi.org/10.1016/j.apradiso.2013.10.004.

[37] M. Uddin, M. Hagiwara, F. Tarkanyi, F. Ditroi, and M. Baba, "Experimental studies on the proton-induced activation reactions of molybdenum in the energy range 22–67MeV", Applied Radiation and Isotopes **60**, 911–920 (2004) https://doi.org/10.1016/j.apradiso.2004.02.004.

[38] H. Piel, S. M. Qaim, and G. Stöcklin, "Excitation Functions of (p,xn)-Reactions on ^{nat}Ni and Highly Enriched ^{62}Ni: Possibility of Production of Medically Important Radioisotope ^{62}Cu at a Small Cyclotron", Radiochimica Acta **57**, 1–6 (1992) doi:10.1524/ract.1992.57.1.1.

[39] *Talys (software), version 1.9, 2018*, http://www.talys.eu/home/.

[40] A. J. Koning, S. Hilaire, and M. C. Duijvestijn, "Talys: comprehensive nuclear reaction modeling", AIP Conference Proceedings **769**, 1154–1159 (2005) 10.1063/1.1945212.

[41] A.A. Ahmed, A. Wrońska, A. Magiera, M. Bartyzel, J.W. Mietelski, R. Misiak, B. Wąs, "Reexamination of Proton-induced Reactions on ^{nat}Mo at 19–26 MeV and Study of Target Yield of Resultant Radionuclides", Acta Physica Polonica B **50**, 1583–1596 (2019).

[42] A. A. Ahmed, A. Wrońska, A. Magiera, R. Misiak, M. Bartyzel, J. W. Mietelski, and B. Wąs, "Study of ^{99}Mo and long-lived impurities produced through (p, x) reactions in the ^{nat}Mo", Radiation Physics and Chemistry **190**, 1–7 (2021) https://doi.org/10.1016/j.radphyschem.2021.109774.

[43] *Experimental nuclear reaction data (EXFOR). Database version of August 29.2020.* https://www-nds.iaea.org/exfor/exfor.htm.

[44] M. Khandaker, M. Uddin, K. Kim, Y. Lee, and G. Kim, "Measurement of cross-sections for the (p, xn) reactions in natural molybdenum", Nuclear Instruments and Methods in Physics Research Section B: Beam Interactions with Materials and Atoms **262**, 171–181 (2007) https://doi.org/10.1016/j.nimb.2007.05.028.

[45] F. Tárkányi, F. Ditrói, A. Hermanne, S. Takács, and A. Ignatyuk, "Investigation of activation cross-sections of proton induced nuclear reactions on ^{nat}Mo up to 40 MeV: New data and evaluation", Nuclear Instruments and Methods in Physics Research Section B: Beam Interactions with Materials and Atoms **280**, 45–73 (2012) https://doi.org/10.1016/j.nimb.2012.02.029.

[46] A. Elbinawi, M. Al-abyad, I. Bashter, U. Seddik, and F. Ditrói, "Study of proton induced nuclear reactions on molybdenum: cross section measurements and theoretical calculations", Radiochimica Acta **108**, 1–9 (2020) https://doi.org/10.1515/ract-2020-frontmatter1.

[47] M. Bonardi, C. Birattari, F. Groppi, and E. Sabbioni, "Thin-target excitation functions, cross-sections and optimised thick-target yields for ^{nat}Mo(p,xn)$^{94g,95m,95g,96(m+g)}$Tc nuclear reactions induced by protons from threshold up to 44 MeV. No Carrier Added radiochemical separation and quality control", Applied Radiation and Isotopes **57**, 617–635 (2002) https://doi.org/10.1016/S0969-8043(02)00176-8.

[48] M. Khandaker, A. M. H. Meaze, K. Kim, D. Son, G. Kim, and Y. Lee, "Measurements of proton-induced reaction cross-sections of ^{nat}Mo by using the MC50 cyclotron at the Korean institute of radiological and medical sciences", J. Korean Physical Society **48**, 821–826 (2006).

[49] A. Alharbi, J. Alzahrani, and A. Azzam, "Activation cross-section measurements of some proton induced reactions on Ni, Co and Mo for proton activation analysis (PAA) purposes", Radiochim. Acta **99**, 763–770 (2011) https://doi.org/10.1524/ract.2011.1885.

[50] A. A. Alharbi, A. Azzam, M. McCleskey, B. Roeder, A. Spiridon, E. Simmons, V. Goldberg, A. Banu, L. Trache, and R. Tribble, "Medical radioisotopes production: a comprehensive cross-section study for the production of Mo and Tc radioisotopes via proton induced nuclear reactions on ^{nat}Mo", Radioisotopes - Applications in Bio-Medical Science. Prof. Nirmal Singh (Ed.), 3–26 (2011).

[51] F. Tárkányi, A. V. Ignatyuk, A. Hermanne, R. Capote, B. V. Carlson, J. W. Engle, M. A. Kellett, T. Kibedi, G. N. Kim, F. G. Kondev, M. Hussain, O. Lebeda, A. Luca, Y. Nagai, H. Naik, A. L. Nicols, F. M. Nortier, S. V. Suryanarayana, S. Takács, and M. Verpelli, "Recommended nuclear data for medical radioisotope production: diagnostic gamma emitters", Journal of Radioanalytical and Nuclear Chemistry **319**, 487–531 (2019) https://doi.org/10.1007/s10967-018-6142-4.

[52] B. Scholten, R. Lambrecht, M. Cogneau, H. Ruiz, and S. Qaim, "Excitation function for the cyclotron production of ^{99m}Tc and ^{99}Mo", Applied Radiation and Isotopes **51**, 69–80 (1999) 10.1016/S0969-8043(98)00153-5.

[53] A. A. Ahmed, A. Wrońska, A. Magiera, A. Curcio, M. Jaglarz, and A. Wawrzyniak, "Study of ^{99}Mo and long-lived impurities produced in the $^{\text{nat}}$Mo(γ, x) reactions using an electron beam", Radiation Physics and Chemistry **177**, 1–6 (2020) https://doi.org/10.1016/j.radphyschem.2020.109095.

[54] D. R. McAlister and E. P. Horwitz, "Automated two column generator systems for medical radionuclides", Applied Radiation and Isotopes **67**, 1985–1991 (2009) https://doi.org/10.1016/j.apradiso.2009.07.019.

[55] *Handbook on photonuclear data for applications cross-sections and spectra*, https://www.iaea.org/publications/6043/handbook-on-photonuclear-data-for-applications-cross-sections-and-spectra, Vienna.

[56] M. Chadwick, P. Obložinský, M. Herman, N. Greene, R. McKnight, D. Smith, P. Young, R. MacFarlane, G. Hale, S. Frankle, A. Kahler, T. Kawano, R. Little, D. Madland, P. Moller, R. Mosteller, P. Page, P. Talou, H. Trellue, M. White, W. Wilson, R. Arcilla, C. Dunford, S. Mughabghab, B. Pritychenko, D. Rochman, A. Sonzogni, C. Lubitz, T. Trumbull, J. Weinman, D. Brown, D. Cullen, D. Heinrichs, D. McNabb, H. Derrien, M. Dunn, N. Larson, L. Leal, A. Carlson, R. Block, J. Briggs, E. Cheng, H. Huria, M. Zerkle, K. Kozier, A. Courcelle, V. Pronyaev, and S. van der Marck, "ENDF/B-VII.0: Next Generation Evaluated Nuclear Data Library for Nuclear Science and Technology",

Nuclear Data Sheets **107**, 2931–3060 (2006) https://doi.org/10.1016/j.nds.2006.11.001.

[57] K. Shibata, O. Iwamoto, T. Nakagawa, N. Iwamoto, A. Ichihara, S. Kunieda, S. Chiba, K.Furutaka, N. Otuka, T. Ohsawa, T. Murata, H. Matsunobu, A. Zukeran, S. Kamada, and J. Karakura, "Jendl-4.0: a new library for nuclear science and engineering", Journal of Nuclear Science and Technology **48**, 1–30 (2011) https://doi.org/10.1080/18811248.2011.9711675.

[58] A. Koning and D. Rochman, "Modern nuclear data evaluation with the talys code system", Nuclear Data Sheets **113**, 2841–2934 (2012) https://doi.org/10.1016/j.nds.2012.11.002.

[59] T. M. Martin, T. Harahsheh, B. Munoz, Z. Hamoui, R. Clanton, J. Douglas, P. Brown, and G. Akabani, "Production of ^{99}Mo/^{99m}Tc via photoneutron reaction using natural molybdenum and enriched ^{100}Mo: part 1, theoretical analysis", Journal of Radioanalytical and Nuclear Chemistry **314**, 1051–1062 (2017) https://doi.org/10.1007/s10967-017-5455-z.

[60] M. Gumiela, J. Dudek, and A. Bilewicz, "New precipitation method for isolation of ^{99m}Tc from irradiated ^{100}Mo target", Journal of Radioanalytical and Nuclear Chemistry **310**, 1061–1067 (2016) 10.1007/s10967-016-4967-2.

[61] *Particle Accelerator Around the World*, http://www-elsa.physik.uni-bonn.de/accelerator_list.html, 2019.

[62] *Light Sources Organisation*, https://lightsources.org, 2020.